# Transcription establishes microenvironments that organize euchromatin

Lennart Hilbert[1,2,3], Yuko Sato[4], Hiroshi Kimura[4], Frank Jülicher[1,3,5], Alf Honigmann[2], Vasily Zaburdaev[1,3,&], Nadine Vastenhouw[2,&,*]

[1]Center for Systems Biology Dresden, 01307 Dresden, Germany; [2]Max Planck Institute of Molecular Cell Biology and Genetics, 01307 Dresden, Germany; [3]Max Planck Institute for the Physics of Complex Systems, 01187 Dresden, Germany; [4]Tokyo Institute of Technology, 226-8503 Yokohama, Kanagawa, Japan; [5]Center for Advancing Electronics Dresden, Technical University Dresden, 01062 Dresden; [&]These authors contributed equally;
*Corresponding author and lead contact: vastenhouw@mpi-cbg.de

## Graphical abstract

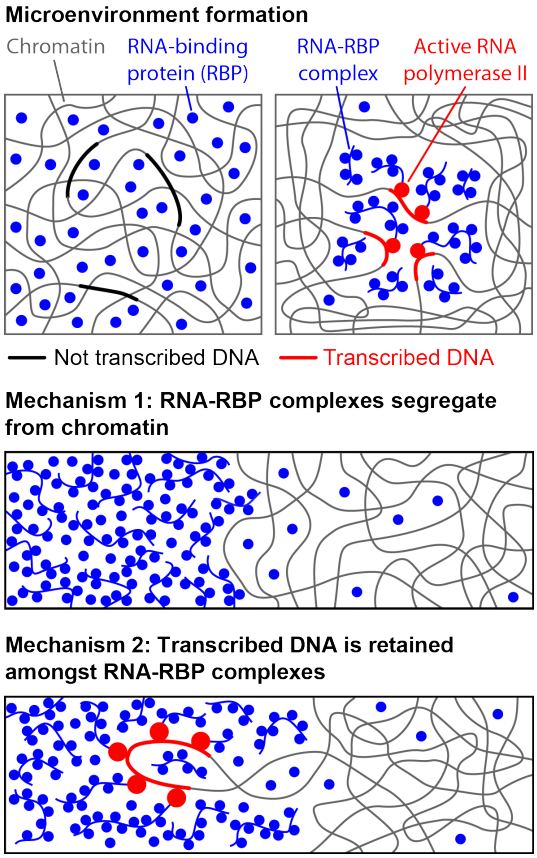


## Highlights

- Transcription establishes microenvironments that remodel euchromatin
- Microenvironments form by RNA accumulation in the vicinity of transcription sites
- Microenvironments exclude not transcribed DNA and retain transcribed DNA
- Euchromatin is organized like an active microemulsion, stabilized by transcription

## Summary

The three-dimensional organization of the genome is essential for development and health. Although the organization of euchromatin (transcriptionally permissive chromatin) dynamically adjusts to changes in transcription, the underlying mechanisms remain elusive. Here, we studied how transcription organizes euchromatin, using experiments in zebrafish embryonic cells and theory. We show that transcription establishes an interspersed pattern of chromatin domains and RNA-enriched microenvironments. Specifically, accumulation of RNA in the vicinity of transcription sites creates microenvironments that locally remodel chromatin by displacing not transcribed chromatin. Ongoing transcriptional activity stabilizes the interspersed pattern of chromatin domains and RNA-enriched microenvironments by establishing contacts between chromatin and RNA. We explain our observations with an active microemulsion model based on two macromolecular mechanisms: RNA/RNA-binding protein complexes generally segregate from chromatin, while transcribed chromatin is retained among RNA/RNA-binding protein accumulations. We propose that microenvironments might be central to genome architecture and serve as gene regulatory hubs.

## Keywords

Nuclear Architecture, Genome Organization, Super-resolution Microscopy, Self-organization, Phase Separation, RNA Polymerase, miR-430

## Introduction

In eukaryotes, DNA is packed inside the cell nucleus in the form of chromatin, which consists of DNA, proteins such as histones, and RNA. During the interphase of the cell cycle, when DNA is transcribed into RNA, chromatin exhibits a dynamic, three-dimensional organization (Cremer and Cremer, 2001; Pombo and Branco, 2007; Nagano *et al.*, 2017; Nozaki *et al.*, 2017). Although chromatin organization has often been described in terms of structures with discrete length scales, recent work has suggested that it is characterized by a continuum of packing densities (Ricci *et al.*, 2015; Ou *et al.*, 2017). This raises the question how such packing is achieved. In the case of heterochromatin, which is transcriptionally repressed, organization can be explained by phase separation (Larson *et al.*, 2017; Strom *et al.*, 2017). For euchromatin, the transcriptionally permissive part of chromatin, spatial organization is required in development and health (Lupiáñez *et al.*, 2015; Flavahan *et al.*, 2016; Hnisz *et al.*, 2016; Symmons *et al.*, 2016), but a mechanism of euchromatin organization has not yet been described.

While the mechanism of euchromatin organization is unclear, it is clear that transcription plays a role. Most dramatically, global inhibition of transcription induces a general compaction of interphase chromatin (Nickerson *et al.*, 1989). In agreement with this, transcription at engineered gene arrays leads to chromatin decompaction (Tsukamoto *et al.*, 2000; Müller *et al.*, 2001). Similarly, gene-rich regions and single genes are localized in regions of decompacted chromatin when they are transcribed (Volpi *et al.*, 2000; Chambeyron and Bickmore, 2004; Ferrai *et al.*, 2010). In addition to affecting the degree of chromatin compaction, transcription has long been suggested to result in DNA-DNA contacts (Cook, 1999). Indeed, genome-wide analyses of DNA-DNA contacts have revealed that transcribed elements are enriched amongst these contacts (Beagrie *et al.*, 2017; Rowley *et al.*, 2017). Moreover, long-range contacts between transcribed regions are lost when transcription is inhibited (Schoenfelder *et al.*, 2010; Hug *et al.*, 2017). Taken together, these results show that the degree of chromatin compaction as well as DNA-DNA contacts depend on transcription. The mechanism by which transcription affects euchromatin organization, however, remains unclear.

RNA, the product of transcription, has also been implicated in chromatin organization. Early experiments revealed that RNA is localized to regions of intermediate and low DNA concentration (Monneron and Bernhard, 1969; Fakan and Bernhard, 1971). A causal link between RNA and chromatin organization was first shown by global RNA digestion, which induced nucleus-wide chromatin compaction (Nickerson *et al.*, 1989). Specific RNAs have also been implicated in chromatin organization. For example, the non-coding RNAs Xist and Firre establish chromatin microarchitectures (Engreitz *et al.*, 2013; Hacisuleyman *et al.*, 2014). Furthermore, chromatin associated RNAs are required for efficient oligomerization of SAF-A protein, which results in decompaction of transcribed euchromatin (Nozawa *et al.*, 2017). The above suggests that transcription as well as RNA have roles in the organization of

euchromatin. The underlying mechanisms, however, remain poorly understood.

Here, we determined how transcription and RNA accumulation organize euchromatin inside the nucleus. First, using STED super-resolution microscopy, we found that transcription establishes an interspersed pattern of chromatin domains and RNA-enriched microenvironments. Transcription inhibition experiments revealed that nuclear RNA accumulation is required to form chromatin domains, and that transcriptional activity is required to maintain chromatin domains and RNA-enriched microenvironments in a finely interspersed pattern. Next, we developed a physical model, which reproduces our observations, and further indicates that euchromatin organization is an example of an active microemulsion. According to this model, microenvironments form by RNA accumulation at transcription sites, and displace not transcribed chromatin from the zone of RNA accumulation. Finally, we observed exactly this sequence by live cell microscopy during transcription onset at a highly induced cluster of micro-RNA genes. Together, our results show that transcription establishes architectural microenvironments by local RNA accumulation. These microenvironments organize euchromatin by excluding not transcribed DNA and retaining transcribed DNA.

## Results

### Transcription onset establishes microenvironments that organize euchromatin

To investigate how transcription dynamically organizes euchromatin, we used late blastula zebrafish cells. These cells divide approximately once per hour (Kimmel *et al.*, 1995), allowing the frequent observation of transcription onset and establishment of chromatin organization after mitosis. Similar to other non-differentiated cells (Ahmed *et al.*, 2010; Ricci *et al.*, 2015), late blastula cells exhibit no permanently compacted heterochromatin (SI Figure 1). This simplifies our analysis by limiting it to euchromatin. Late blastula cells also do not have distinguishable nucleoli (Heyn *et al.*, 2016). The absence of nucleoli, which are sites of ribosome biogenesis, removes another complication from the analysis. To allow for the acquisition of two-dimensional, super-resolution fluorescence intensity images of DNA, RNA, and transcriptional activity within nuclei of intact cells, we established a protocol for three-color STED microscopy (SI Figure 2). We could identify the progress of individual cells through transcription onset by nuclear accumulation of RNA and levels of transcriptional activity (SI Figure 3). Thus, the application of STED microscopy to zebrafish late blastula cells allows us to assess euchromatin organization during transcription onset after mitosis.

To assess how transcription contributes to euchromatin organization, we compared microscopy images from cells before and after the onset of transcription (cell selection is documented in SI Figure 4 A-C). We observed that the DNA intensity profile inside nuclei was relatively smooth before transcription onset and that distinct DNA domains were present after

transcription onset (Figure 1 A). We characterized the observed changes in the DNA intensity profile inside nuclei using two quantitative measures. The first measure, image contrast, quantifies how strongly the intensity in different areas of the nucleus differs. After transcription onset, image contrast was significantly increased, reflecting the observed formation of DNA domains (Figure 1 B). The second measure, correlation length, quantifies the length scale of patterns in the intensity profile irrespective of differences in image contrast. The correlation length was approximately 500 nm both before and after transcription onset, indicating that DNA domain formation does not establish patterns exceeding this length scale (Figure 1 C, for correlation functions see SI Figure 6 A, B). To test whether the observed changes require transcription, we inhibited RNA polymerase II activity by α-amanitin. In this case, the formation of DNA domains did not occur (SI Figure 7). These results indicate that RNA polymerase II mediated transcription establishes a DNA domain pattern with a length scale of ~500 nm or less.

To understand how transcription establishes the observed DNA domain pattern, we studied how RNA and transcriptional activity (monitored by labeling elongating RNA polymerase II, Pol II Ser2Phos) are spatially related to DNA domains. We observed that after transcription onset, RNA and transcriptional activity were also localized in distinct domains (Figure 1 D). These domains were localized in DNA-depleted zones (Figure 1 E). Quantitative analysis confirms that the highest intensities of RNA and transcriptional activity occurred in regions of low DNA intensity (Figure 1 F). These observations are in line with previous electron microscopy results (Iborra *et al.*, 1996; Eskiw *et al.*, 2008). We further found low intensity DNA protrusions that reach into the otherwise DNA-depleted zones (Figure 1 E, arrowheads). The peaks of transcriptional activity are located on these DNA protrusions (Figure 1 G, arrowheads). RNA intensity peaks occurred close to the transcriptional activity peaks (Figure 1 G), likely representing transcripts resulting from this transcriptional activity. A two-dimensional analysis that resolved transcriptional activity by DNA and RNA intensity reflected this organization, showing the highest intensity of transcriptional activity in locations with low to intermediate DNA intensity and maximal RNA intensity (Figure 1 H). These results suggest that transcription establishes RNA-enriched domains, or microenvironments. Transcribed DNA protrudes into these microenvironments while not transcribed DNA forms domains that are spatially segregated from the RNA-enriched microenvironments. These results are in line with previous observations of functional nuclear architecture (Cremer and Cremer, 2001; Pombo and Branco, 2007).

### Transcriptional activity and RNA play distinct roles in euchromatin organization

The internal organization of microenvironments (Figure 1 E-H) suggests that transcriptional activity and RNA accumulation might have distinct roles in chromatin organization. To study these roles in more detail, we inhibited transcription by applying flavopiridol. After flavopiridol treatment, transcriptional activity was suppressed and nuclei retained a range of RNA levels, which is likely due to differences in the amount of nuclear RNA at the

time flavopiridol was applied (Figure 2 A). To study the role of transcriptional activity, we selected those cells that retained significant amounts of nuclear RNA (SI Figure 4 D-F). In the nuclei of these cells, RNA was localized to regions with low DNA intensity, as was observed in non-treated cells (Figure 2 B, C). Hence, the segregation into DNA and RNA domains appears to be unaffected by the suppression of transcriptional activity. However, the pattern formed by DNA domains was markedly coarser in nuclei of inhibited cells when compared to nuclei of control cells (Figure 2 D). DNA domains were more pronounced and larger, as reflected by an increased DNA image contrast (Figure 2 E), and an increased correlation length (Figure 2 F), respectively. The observed changes were reversible, indicating that they are not due to toxic side effects of inhibition (SI Figure 8). This suggests that transcriptional activity is not required for the formation of chromatin domains, but to maintain RNA and chromatin domains in a finely interspersed pattern.

We then investigated the role of RNA accumulation in euchromatin organization. The spatial segregation of RNA from chromatin indicates that accumulation of RNA in the nucleus might be required for the confinement of chromatin into distinct domains. Indeed, DNA domains became more pronounced with increasing amounts of RNA in the nucleus (Figure 2 G). Together, these observations show that RNA that accumulates in the nucleus segregates from chromatin and thereby establishes a pattern of segregated chromatin and RNA domains. Transcriptional activity maintains these chromatin and RNA domains in a finely interspersed pattern.

From the above observations, the question arises how transcriptional activity maintains the interspersed pattern of DNA and RNA domains. One possibility is that transcribing RNA polymerase is required, while it also possible that the transcripts associated with RNA polymerase are sufficient. The inhibitor flavopiridol, which we used above, cannot help distinguish between these possibilities because its application results in the loss of transcribing RNA polymerase (Bensaude, 2011; Jonkers, Kwak and Lis, 2014). Here, we applied a different inhibitor, actinomycin-D (Act-D), which arrests RNA polymerases during transcription (Custódio *et al.*, 1999; Bensaude, 2011). The arrested polymerases are temporarily retained along with their associated transcripts, which can be visualized as RNA foci (Custódio *et al.*, 1999). After 30 minutes of Act-D treatment, transcriptional activity was suppressed (SI Figure 9 A), and foci of retained RNA could be observed (SI Figure 9 B). At this time, no change in DNA intensity distributions was detected (Figure 2 H). After 60 minutes of Act-D treatment, RNA foci were no longer observed, indicating the loss of retained RNA (SI Figure 9 B). In this situation, DNA domains became more pronounced (Figure 2 H). These results imply that transcribing RNA polymerases are not required to maintain the interspersed pattern of DNA and RNA domains. Rather, stalled RNA polymerases that keep transcripts in physical contact with DNA maintain the interspersed pattern of DNA and RNA domains.

The experimental results up to this point can be summarized as follows (for a schematic see Figure 2 I). Transcription onset establishes a finely interspersed pattern of mutually exclusive chromatin and RNA domains. This interspersed pattern is maintained by DNA-RNA contacts established via active RNA polymerases. When transcription is inhibited in a manner that removes these DNA-RNA contacts, chromatin and RNA domains are no longer finely interspersed. In nuclei not containing a significant amount of RNA, chromatin does not form domains, irrespective of the application of a transcription inhibitor.

### Physical model of euchromatin organization by transcription

To provide an explanation for our experimental observations, we propose a physical model of euchromatin organization by transcription. This model follows two main components, RNA-binding proteins (RBPs) and chromatin. RBPs occur in two forms: unbound or bound to RNA (forming RNA-RBP complexes). Chromatin occurs in two states: transcribed or not transcribed. We incorporate the two following macromolecular mechanisms into the physical model. First, RNA-RBP complexes segregate from chromatin (Figure 3 A). Second, transcribed chromatin is retained among RNA-RBP complexes (Figure 3 B). The latter is a consequence of the tethering of RNA-RBP complexes to chromatin during the transcription process, resulting in the segregation of transcribed chromatin from chromatin in general. Transitions between transcribed and not transcribed chromatin, as well as between unbound and bound RBP, are represented in a reaction network (Figure 3 C). We simulate the spatiotemporal organization of the macromolecular components using a coarse-grained model, in which the space of interest is divided into discrete compartments. Each compartment is occupied by a single species, which represents the predominant component in this compartment. Coarse-graining makes simulations of large spaces computationally tractable, which would be too computationally intensive when simulated at the molecular level. To achieve acceptable computational performance in our case, we implemented our model as a two-dimensional square lattice (Figure 3 D). The simulation model used to implement the spatiotemporal organization is adapted from an approach originally used for microemulsions (Larson, Scriven and Davis, 1985). In this approach, neighboring compartments stochastically swap contents. The likelihood of a given swap is determined by the required free energy change. A free energy cost is associated with placing RNA-RBP complexes next to chromatin, representing the segregation of RNA-RBP complexes from chromatin (Figure 3 D). Note that, because RNA-RBP complexes are tethered to transcribed chromatin, this free energy cost also applies for the placement of transcribed chromatin next to chromatin in general. To account for the integrity of the linear DNA polymer, swap operations that would break chromatin into disconnected domains are not allowed. Model parameters are assigned from literature (SI, Table 2) or chosen based on our experimental data (SI Figure 10).

We aimed to approximate experimental conditions in our simulations. Our simulations evolve with a fixed time step, so that they can be mapped to the timing of cellular events and experimental manipulations. The state before transcription onset was approximated by simulations with only not transcribed chromatin and unbound RBP. Transcription onset and inhibition are implemented by changing the rate at which chromatin transitions from the not transcribed to the transcribed state. At times of interest, spatial distributions of the simulated species are extracted and converted into concentration profiles of all chromatin, transcribed chromatin, and RNA, which can be compared to microscopy images. Because our simulation model is stochastic, each simulation produces different concentration profiles. We therefore obtained statistical distributions of quantitative features by executing multiple simulations.

### Model simulations reproduce key features of euchromatin organization

To test if the physical model can account for the experimentally observed DNA intensity profiles, we approximated experimental conditions and compared the resulting concentration profiles to our microscopy images. First, to approximate the conditions of a cell before transcription onset, we set the rate at which chromatin transitioned into the transcribed state to zero and executed a number of simulations steps sufficient to equilibrate the system. The concentration of RNA and transcribed chromatin were zero throughout the lattice, and the chromatin concentration profile exhibited no domains (Figure 4 A-C). Then, to approximate the conditions of a cell after transcription onset, we changed the rate at which chromatin transitioned into the transcribed state to a non-zero value. We continued the simulations until the concentration of RNA and transcribed chromatin reached a plateau. Under these conditions, the chromatin concentration profiles exhibited domains (Figure 4 D). Chromatin domains were interspersed with RNA accumulations (Figure 4 E) and transcribed chromatin (Figure 4 F). A corresponding organization was observed in microscopy images from nuclei before and after transcription onset (Figure 1 A and D). Lastly, to approximate transcription inhibition, we returned the rate at which chromatin transitions into the transcribed state to zero. We continued the simulations for a number of steps corresponding to 30 minutes, which was the duration of transcription inhibition in the experiment. In the resulting concentration profiles, a significant concentration of RNA was retained, most chromatin returned to the not transcribed state, and the chromatin pattern was markedly coarsened (Figure 4 G-I). In microscopy images of nuclei in the corresponding situation, a coarsening of the DNA domain pattern was also seen (Figure 2 D). Hence, the simulated chromatin concentration profiles exhibited patterns similar to those observed in our experiments.

To extend our comparison to the quantitative analyses of DNA organization, we applied the same analysis procedures used for microscopy images to chromatin concentration profiles obtained from the above simulations. In agreement with experimental observations, the image contrast increased with simulated transcription onset, and further increased after transcription

inhibition (Figure 4 J). The correlation length increased after transcription inhibition, closely matching the experiment (Figure 4 K, for correlation functions see SI Figure 6). Before transcription onset, image contrast and correlation length in simulations were lower than in experiments, likely reflecting that in a real cell nucleus, processes other than only transcription occur. Together, the assessment of concentration profiles and the quantitative analysis indicate that our physical model accounts for key features of the euchromatin organization observed in our experiments.

**Microenvironments form by RNA accumulation and expel not transcribed DNA**

Considering that microenvironments are an integral part of euchromatin organization (Figure 1), we wanted to understand the dynamic process of microenvironment formation. First, we characterized how a single microenvironment would form according to the physical model. To this end, we simulated transcription onset at a single transcription site in a background of not transcribed chromatin (Figure 5 A). With increasing transcriptional activity, RNA accumulates around the transcription site (Figure 5 B). Simultaneously, most chromatin is displaced from the region where RNA accumulates (Figure 5 C). This displacement specifically affects not transcribed chromatin, while transcribed chromatin is retained within the chromatin-depleted zone (Figure 5 D). The accumulating RNA is localized in the depleted zone (Figure 5 E). Spatiotemporal analysis shows that this sequence of events is conserved across simulations (Figure 5 F-H). Thus, according to the physical model, microenvironments form by RNA accumulation as a result of transcription onset, and displace not transcribed chromatin.

Next, we assessed microenvironment formation in live cells. To that end, we searched for isolated transcription sites. We identified two prominent transcription sites, that occur throughout practically all nuclei of late blastula zebrafish embryos (Figure 6 A, B). Transcription of these sites preceded the nucleus-wide transcription onset after mitosis (Figure 6 C). Previous work revealed that the *miR-430* gene cluster is very highly transcribed in late blastula zebrafish embryos (Heyn et al., 2014). We detected primary miR-430 transcripts at the prominent transcription sites, suggesting a role for miR-430 transcription in their formation (SI Figure 11). To follow potential DNA remodeling at these sites by microscopy with sufficient optical resolution, we cultured embryonic cells in a refractive index-matched medium that we recently developed (Boothe *et al.*, 2017). We monitored promoter-recruited RNA polymerase II as well as elongating RNA polymerase II by live cell-compatible antibody fragments (Hayashi-Takanaka *et al.*, 2011; Stasevich, Hayashi-Takanaka, *et al.*, 2014). We found that RNA polymerase II recruitment first occurred at two sites (Figure 7 A). A few minutes after their occurrence, these sites acquired signal for transcription elongation (Figure 7 B). Concurrently, DNA was displaced (Figure 7 C). Spatiotemporal analysis across multiple nuclei indicated that this sequence is highly reproducible (Figure 7 D-F). Fixed cell microscopy revealed that RNA accumulates with increasing transcriptional activity, and transcribed DNA is retained within the

newly forming microenvironments (Figure 7 G-K). Hence, in live cells as well as in model simulations, microenvironments are established by RNA accumulation, displace not transcribed DNA, and retain transcribed DNA.

## Discussion

In this study, we have shown that transcription establishes RNA-enriched microenvironments, which organize euchromatin by excluding not transcribed chromatin and retaining transcribed chromatin. Nuclear accumulation of RNA as well as ongoing transcriptional activity play a key role in maintaining a finely interspersed pattern of chromatin domains and RNA-enriched microenvironments. We explain our observations with a physical model based on two macromolecular mechanisms: segregation of RNA-RBP complexes from chromatin, and retention of transcribed chromatin among RNA-RBP complexes.

### RNA accumulation and transcriptional activity establish functional architecture

The euchromatin organization we observed is in agreement with the functional nuclear architecture seen in various cell types (Cremer and Cremer, 2001; Pombo and Branco, 2007). Specifically, chromatin and RNA form a pattern of segregated but finely interspersed domains, and transcribed DNA is localized in regions of RNA accumulation. Our results reveal how transcription establishes this functional architecture. First, nuclear accumulation of RNA is required to establish distinct chromatin domains. These chromatin domains form by segregation of accumulating RNA from chromatin. In our physical model, RBPs that are bound by RNA segregate from chromatin. Note that, from a physical perspective, such segregation can be seen as a phase separation (Brangwynne *et al.*, 2009; Hyman, Weber and Jülicher, 2014). Second, transcriptional activity is required to maintain RNA and chromatin domains in a finely interspersed pattern. The maintenance of this pattern relies on the tethering of RNA to transcribed DNA, which establishes connections between RNA and chromatin domains. In our physical model, the tethered RNA forms RNA-RBP complexes, so that transcribed DNA is retained in regions of RNA-RBP accumulation. From a physical perspective, the connections between RNA and DNA domains prevent a full phase separation.

### Euchromatin organization is an example of an active microemulsion

The process of euchromatin organization described by our physical model is similar to a microemulsion. Conventional microemulsions consist of two phases, often a hydrophobe and a hydrophile, and an amphiphile with affinity for both phases (Davis *et al.*, 1987). The amphiphile, for example a detergent, reduces the surface tension between the two phases, resulting in a dramatic increase of interface area between the phases. Thus, increasing amphiphile concentration induces increasingly fine dispersion patterns. At insufficient amphiphile concentrations, the two phases separate into a coarse pattern. In our physical model, RNA-RBP complexes and chromatin are the two separating phases. During transcription elongation, RNA polymerase tethers RNA-RBP complexes to transcribed DNA, thus creating an amphiphile.

Because the amount of this amphiphile is proportional to transcriptional activity, RNA-RBP and chromatin domains are finely interspersed at high transcription levels, and form a coarse pattern when transcription is inhibited. Different from a conventional microemulsion, the amphiphile in our model synthesizes RNA transcripts, which convert freely diffusing RBPs into RNA-RBP complexes that segregate from chromatin. Hence, euchromatin organization can be described as an active microemulsion, which is stabilized by amphiphiles that produce one of the phases.

### Microenvironments might explain major features of genome architecture

Our finding that transcribed DNA is localized in microenvironments is in line with suggestions that transcribed genes colocalize (Cook, 1999). Such a colocalization of transcribed DNA is supported by recent studies of DNA-DNA contacts. For example, DNA-DNA contacts are significantly enriched in highly transcribed DNA elements (Rao *et al.*, 2014; Beagrie *et al.*, 2017), transcription levels predict DNA-DNA contact frequencies (Rowley *et al.*, 2017), and long-range DNA-DNA contacts depend on ongoing transcription (Hug *et al.*, 2017). At the megabase scale, the genome can be assigned to regions that are defined by an elevated internal contact frequency (Lieberman-Aiden *et al.*, 2009). Based on contacts between these regions, they can be assigned to two compartments, A and B: A regions mostly contact A regions, B regions mostly contact B regions. A and B compartments are highly correlated with transcriptionally active and inactive chromatin, respectively. The compartments are also segregated in three-dimensional space (Wang *et al.*, 2016; Di Pierro *et al.*, 2017), which is similar to the spatial segregation of transcribed from not transcribed chromatin we observed. Thus, the formation of microenvironments by transcription might explain the colocalization of transcribed DNA elements as well as A/B compartmentalization.

### Microenvironments might be hubs of gene regulation

Previous work has described microenvironments in the context of gene regulation (Zaidi *et al.*, 2005). These microenvironments are characterized by high concentrations of transcription factors that can potentiate the induction of target genes (Mir *et al.*, 2017; Tsai *et al.*, 2017). The localization of genes to accumulations of transcription factors (Papantonis *et al.*, 2012; Liu *et al.*, 2014) might also explain observations of proximity-based gene regulation (Fanucchi *et al.*, 2013). Our work explains how transcription establishes microenvironments that can retain several transcribed genes and potentially facilitate the accumulation of transcription factors.

To conclude, we have shown how transcription establishes microenvironments that spatially organize euchromatin. This organization is similar to an active microemulsion. This mechanistic insight might provide a context in which to understand the emergence of many features of nuclear organization and the spatial organization of gene regulation.

## Acknowledgements

This work was supported by the Max Planck Society, a Human Frontier Science Program career development award (to N.V., CDA-00060/2012), an ELBE Postdoctoral Fellowship from the Center for Systems Biology Dresden (to L.H.), the Volkswagen foundation (to V.Z.), JSPS KAKENHI Grants JP15K07157 (to Y.S.) and JP25116005, JP26291071, and JP17H01417 (to H.K.). We thank Antonius van Boxtel for *in situ* probes, Jan Brugues, Shai Joseph, Máté Pálfy, Iain Patten, Wolfram Poenisch, Jaques Prost, Thomas Quail, Rabea Seyboldt, Carine Stapel, and Christoph Weber for discussions, Jochen Rink for comments on our manuscript, and the following facilities and services: fish facility (MPI-CBG), light microscopy facility (MPI-CBG), computer department (MPI-CBG and MPI-PKS).

## Author contributions

Conceptualization, L.H., N.V., V.Z. and F.J.; Methodology, L.H., A.H. and V.Z.; Software, L.H.; Formal Analysis, L.H.; Investigation, L.H.; Resources – Y.S. and H.K.; Writing – Original Draft, L.H., N.V. and V.Z.; Writing – Review & Editing, L.H., N.V., V.Z., A.H., H.K. and F.J.; Supervision – N.V., V.Z.; Funding Acquisition – L.H., Y.S., H.K., F.J., A.H., V.Z. and N.V.

## References

Ahmed, K. *et al.* (2010) Global chromatin architecture reflects pluripotency and lineage commitment in the early mouse embryo, *PLoS ONE*, 5(5), e10531.
Bahar Halpern, K. *et al.* (2015) Nuclear Retention of mRNA in Mammalian Tissues, *Cell Reports*, 13(12), 2653–2662.
Battich, N., Stoeger, T. and Pelkmans, L. (2015) Control of Transcript Variability in Single Mammalian Cells, *Cell*, 163(7), 1596–1610.
Beagrie, R. A. *et al.* (2017) Complex multi-enhancer contacts captured by genome architecture mapping, *Nature*, 543(7646), 519–524.
Bensaude, O. (2011) Inhibiting eukaryotic transcription: Which compound to choose? How to evaluate its activity?, *Transcription*, 2(3), 103–108.
Boothe, T. *et al.* (2017) A tunable refractive index matching medium for live imaging cells, tissues and model organisms, *eLife*, 6, e27240.
van Boxtel, A. L. *et al.* (2015) A Temporal Window for Signal Activation Dictates the Dimensions of a Nodal Signaling Domain, *Developmental Cell*, 35(2), 175–185.
Brangwynne, C. *et al.* (2009) Germline P Granules are Liquid Droplets that Localize by Controlled Dissolution/Condensation, *Science*, 324(5935), 1729–1732.
Chambeyron, S. and Bickmore, W. A. (2004) Chromatin decondensation and nuclear reorganization of the HoxB locus upon induction of transcription, *Genes and Development*, 18(10), 1119–1130.
Cook, P. R. (1999) The Organization of Replication and Transcription, *Science*, 284(5421), 1790–1795.
Cremer, T. and Cremer, C. (2001) Chromosome Territories, Nuclear Architecture and Gene Regulation in Mammalian Cells, *Nature Reviews Genetics*, 2(4), 292–301.
Custódio, N. *et al.* (1999) Inefficient processing impairs release of RNA from the site of transcription, *EMBO Journal*, 18(10), 2855–2866.
Davis, H. T. *et al.* (1987) Microemulsions and Their Precursors, *Physics of Amphiphilic Layers*, 21, 310–327.
Engreitz, J. M. *et al.* (2013) The Xist lncRNA exploits three-dimensional genome architecture to spread across the X chromosome, *Science*, 341(6147), 1237973.
Eskiw, C. H. *et al.* (2008) RNA polymerase II activity is located on the surface of protein-rich transcription factories, *Journal of Cell Science*, 121(12), 1999–2007.
Fakan, S. and Bernhard, W. (1971) Localisation of rapidly and slowly labelled nuclear RNA as visualized by high resolution autoradiography, *Experimental Cell Research*, 67(1), 129–141.
Fanucchi, S. *et al.* (2013) Chromosomal Contact Permits Transcription between Coregulated Genes, *Cell*, 155(3), 606–620.
Ferrai, C. *et al.* (2010) Poised transcription factories prime silent uPA gene prior to activation, *PLoS Biology*, 8(1), e1000270.
Flavahan, W. A. *et al.* (2016) Insulator dysfunction and oncogene activation in IDH mutant gliomas, *Nature*, 529(7584), 110–114.
Goldberg, I. G. *et al.* (2005) The Open Microscopy Environment (OME) Data

Model and XML file: open tools for informatics and quantitative analysis in biological imaging, *Genome Biology*, 6(5), R47.
Hacisuleyman, E. *et al.* (2014) Topological organization of multichromosomal regions by the long intergenic noncoding RNA Firre, *Nature Structural and Molecular Biology*, 21(2), 198–206.
Hayashi-Takanaka, Y. *et al.* (2011) Tracking epigenetic histone modifications in single cells using Fab-based live endogenous modification labeling, *Nucleic Acids Research*, 39(15), 6475–6488.
Heyn, P. *et al.* (2014) The earliest transcribed zygotic genes are short, newly evolved, and different across species, *Cell Reports*, 6(2), 285–292.
Heyn, P. *et al.* (2016) Activation of transcription enforces the formation of distinct nuclear bodies in zebrafish embryos, *RNA Biology*, 14(6), 752–760.
Hnisz, D. *et al.* (2016) Activation of proto-oncogenes by disruption of chromosome neighborhoods, *Science*, 351(6280), 1454–1458.
Hug, C. B. *et al.* (2017) Chromatin Architecture Emerges during Zygotic Genome Activation Independent of Transcription, *Cell*, 169(2), 216–228.
Hyman, A. A., Weber, C. A. and Jülicher, F. (2014) Liquid-liquid Phase Separation in Biology, *Annual Reviews in Cell and Developmental Biology*, 30, 39–58.
Iborra, F. J. *et al.* (1996) Active RNA polymerases are localized within discrete transcription 'factories' in human nuclei, *Journal of Cell Science*, 109(6), 1427–1436.
Jonkers, I., Kwak, H. and Lis, J. T. (2014) Genome-wide dynamics of Pol II elongation and its interplay with promoter proximal pausing, chromatin, and exons, *eLife*, 3, e02407.
Joseph, S. R. *et al.* (2017) Competition between histone and transcription factor binding regulates the onset of transcription in zebrafish, *eLife*, 6, e23326.
Kimmel, C. B. *et al.* (1995) Stages of embryonic development of the zebrafish, *Developmental Dynamics*, 203(3), 253–310.
Kimura, H. and Yamagata, K. (2015) Visualization of Epigenetic Modifications in Preimplantation Embryos, in *Methods in Molecular Biology*, 127–148.
Larson, A. G. *et al.* (2017) Liquid droplet formation by HP1α suggests a role for phase separation in heterochromatin, *Nature*, 547(7662), 236–240.
Larson, R. G., Scriven, L. E. and Davis, H. T. (1985) Monte Carlo simulation of model amphiphile-oil–water systems, *Journal of Chemical Physics*, 83(5), 2411–2420.
Lee, M. T. *et al.* (2013) Nanog, Pou5f1 and SoxB1 activate zygotic gene expression during the maternal-to-zygotic transition, *Nature*, 503(7476), 360–364.
Lieberman-Aiden, E. *et al.* (2009) Comprehensive Mapping of Long-Range Interactions Reveals Folding Principles of the Human Genome, *Science*, 326(5950), 289–294.
Liu, Z. *et al.* (2014) 3D imaging of Sox2 enhancer clusters in embryonic stem cells, *eLife*, 3, e04236.
Lupiáñez, D. G. *et al.* (2015) Disruptions of topological chromatin domains cause pathogenic rewiring of gene-enhancer interactions, *Cell*, 161(5), 1012–1025.

Mir, M. *et al.* (2017) Dense Bicoid Hubs Accentuate Binding along the Morphogen Gradient, *Genes and Development*, 31(17), 1784–1794.
Monneron, A. and Bernhard, W. (1969) Fine structural organization of the interphase nucleus in some mammalian cells, *Journal of Ultrastructure Research*, 27(3–4), 266–288.
Müller, W. G. *et al.* (2001) Large-scale chromatin decondensation and recondensation regulated by transcription from a natural promoter, *Journal of Cell Biology*, 154(1), 33–48.
Nagano, T. *et al.* (2017) Cell-cycle dynamics of chromosomal organization at single-cell resolution, *Nature*, 547(7661), 61–67.
Nickerson, J. A. *et al.* (1989) Chromatin architecture and nuclear RNA, *Proceedings of the National Academy of Sciences USA*, 86(1), 177–181.
Nozaki, T. *et al.* (2017) Dynamic Organization of Chromatin Domains Revealed by Super-Resolution Live-Cell Imaging, *Molecular Cell*, 67(2), 282–293.e7.
Nozawa, R.-S. *et al.* (2017) SAF-A regulates interphase chromosome structure through oligomerisation with chromatin-associated RNAs, *Cell*, 169(7), 1214–1227.
Ou, H. D. *et al.* (2017) ChromEMT: Visualizing 3D chromatin structure and compaction in interphase and mitotic cells, *Science*, 357(6349).
Papantonis, A. *et al.* (2012) TNFα signals through specialized factories where responsive coding and miRNA genes are transcribed, *EMBO Journal*, 31(23), 4404–14.
Di Pierro, M. *et al.* (2017) De Novo Prediction of Human Chromosome Structures: Epigenetic Marking Patterns Encode Genome Architecture, *Proceedings of the National Academy of Sciences USA*.
Pombo, A. and Branco, M. R. (2007) Functional organisation of the genome during interphase, *Current Opinion in Genetics and Development*, 17(5), 451–5.
Rao, S. S. P. *et al.* (2014) A 3D map of the human genome at kilobase resolution reveals principles of chromatin looping, *Cell*, 159(7), 1665–1680.
Ricci, M. A. *et al.* (2015) Chromatin Fibers Are Formed by Heterogeneous Groups of Nucleosomes In Vivo, *Cell*, 160(6), 1145–1158.
Rowley, M. J. *et al.* (2017) Evolutionarily Conserved Principles Predict 3D Chromatin Organization, *Molecular Cell*, 67(5), 837–852.
Schindelin, J. *et al.* (2012) Fiji: an open-source platform for biological-image analysis, *Nature Methods*, 9(7), 676–82.
Schoenfelder, S. *et al.* (2010) Preferential associations between co-regulated genes reveal a transcriptional interactome in erythroid cells, *Nature Genetics*, 42(1), 53–61.
Stasevich, T. J., Sato, Y., *et al.* (2014) Quantifying histone and RNA polymerase II post-translational modification dynamics in mother and daughter cells, *Methods*, 70(2–3), 77–88.
Stasevich, T. J., Hayashi-Takanaka, Y., *et al.* (2014) Regulation of RNA polymerase II activation by histone acetylation in single living cells, *Nature*, 516(7530), 272–275.
Strom, A. R. *et al.* (2017) Phase separation drives heterochromatin domain formation, *Nature*, 547(7662), 241–245.

Symmons, O. *et al.* (2016) The Shh Topological Domain Facilitates the Action of Remote Enhancers by Reducing the Effects of Genomic Distances, *Developmental Cell*, 39(5), 529–543.
Tsai, A. *et al.* (2017) Nuclear microenvironments modulate transcription from low-affinity enhancers, *eLife*, 6, e28975.
Tsukamoto, T. *et al.* (2000) Visualization of gene activity in living cells, *Nature Cell Biology*, 2(12), 871–878.
Vagenende, V. *et al.* (2013) Quantifying the Molecular Origins of Opposite Solvent Effects on Protein-Protein Interactions, *PLoS Computational Biology*, 9(5), e1003072.
Volpi, E. V *et al.* (2000) Large-scale chromatin organization of the major histocompatibility complex and other regions of human chromosome 6 and its response to interferon in interphase nuclei, *Journal of Cell Science*, 113(9), 1565–1576.
Wada, Y. *et al.* (2009) A wave of nascent transcription on activated human genes, *Proceedings of the National Academy of Sciences USA*, 106(43), 18357–18361.
Wang, S. *et al.* (2016) Spatial organization of chromatin domains and compartments in single chromosomes, *Science*, 353(6299), 598–602.
Zaidi, S. K. *et al.* (2005) The dynamic organization of gene-regulatory machinery in nuclear microenvironments, *EMBO Reports*, 6(2), 128–133.

# Figures

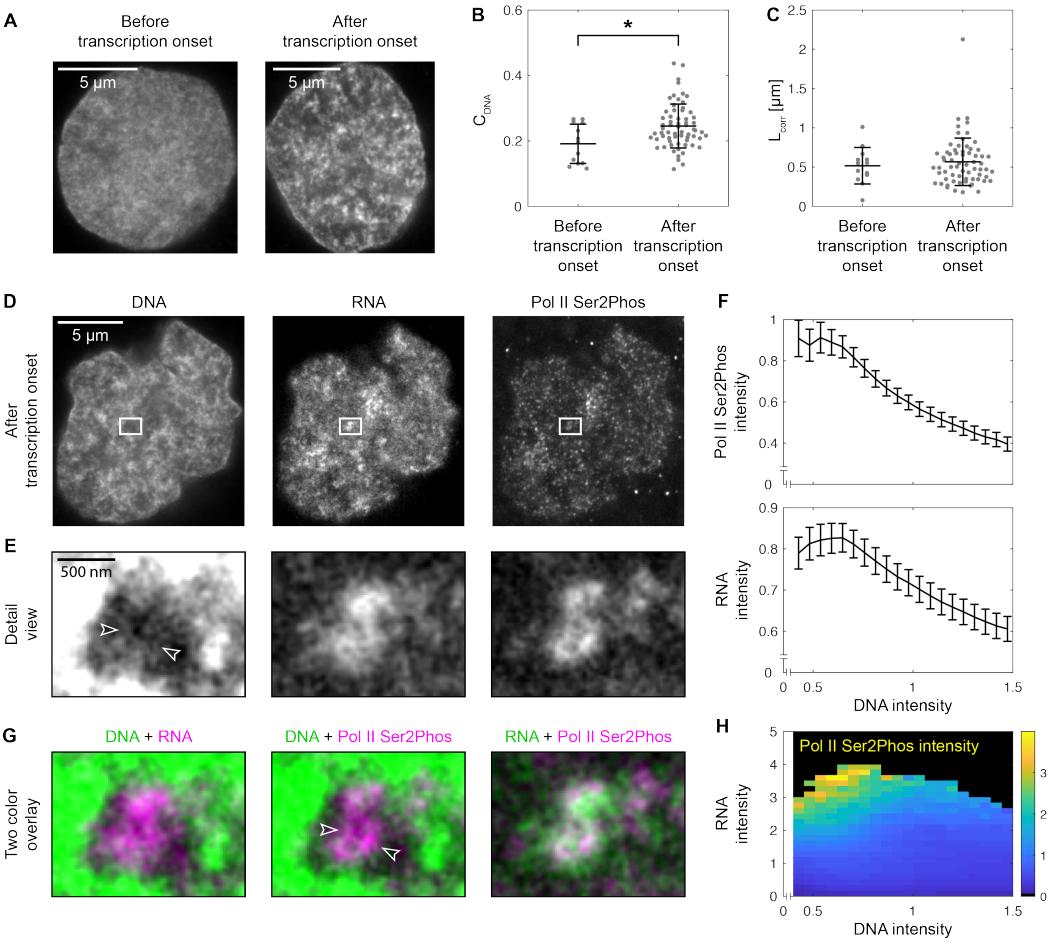


**Figure 1: Transcription onset after mitosis establishes microenvironments that organize euchromatin.** Nuclear mid-section images were acquired by three-color STED super-resolution microscopy and sorted into those from cells before and after transcription onset (SI Figure 4 A-C). **A)** DNA images show relatively uniform intensity distributions before transcription onset and a pattern of DNA-rich domains after transcription onset. **B)** The presence of DNA domains after transcription onset is reflected by an increase in DNA image contrast ($C_{DNA}$). Individual values with mean±SD, * indicates $p<0.05$, permutation test (n = 13, 66). **C)** The formation of DNA domains does not increase organization at long length scales, reflected by an unchanged correlation length ($L_{corr,}$ for radial correlation functions, see SI Figure 6). Plotting and statistics same as panel B, no significant difference detected. **D)** RNA and transcriptional activity (monitored by RNA Pol II Ser2Phos signal) are localized to regions of low DNA intensity. **E**) Zooming into images reveals DNA-depleted microenvironments that contain RNA and Pol II Ser2Phos. Low intensity DNA protrusions into the otherwise DNA-depleted zones could be observed (arrowheads). **F)** The localization of high Pol II Ser2Phos and RNA intensity to regions of low DNA intensity is also seen in a quantitative analysis. Pol II Ser2Phos and RNA intensity are cytoplasm-subtracted and normalized so that a value of 1 corresponds to the highest detected intensities. DNA intensity is normalized by the mean DNA intensity inside a given cell nucleus, and limited to a range where reliable analysis was possible (SI Figure 5). Plots are mean±SEM. **G)** Two-color merge images show that (i) RNA is localized within the DNA-depleted zones, (ii) Pol II Ser2Phos is localized to the DNA protrusions (arrowheads), and (iii) RNA peaks colocalize with Pol II Ser2Phos (white color indicates colocalization of green and magenta signal). **H)** Resolving Pol II Ser2Phos intensity by DNA and RNA intensity reveals that transcriptional activity occurs preferentially in areas of low DNA intensity and high RNA intensity.

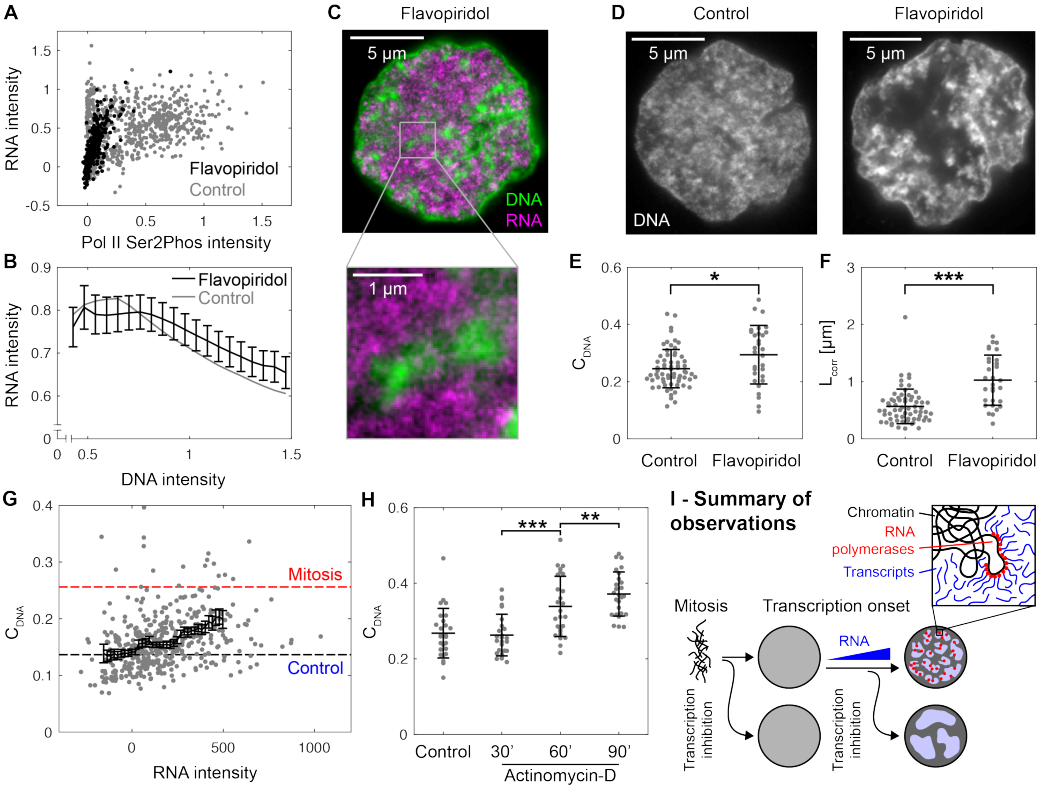


**Figure 2: Transcription inhibition reveals distinct roles of transcriptional activity and RNA accumulation. A)** Treatment with flavopiridol for 30 minutes suppresses transcriptional activity, but cells retain a range of nuclear RNA concentrations. Data points represent single nuclei, images recorded by spinning disk confocal microscopy. **B)** In nuclei of flavopiridol-treated cells that retain RNA (for cell selection, see SI Figure 4 D-F), RNA is localized to regions of low DNA intensity. **C)** Representative STED super-resolution microscopy mid-section of the nucleus of a flavopiridol-treated cell, showing segregation of DNA from RNA. **D)** The DNA domains are markedly coarser in nuclei after flavopiridol treatment compared to nuclei in control-treated cells. **E)** Coarsening of DNA domains after flavopiridol treatment is reflected by an increase in $C_{DNA}$. Individual values with mean±SD. * indicates p<0.05, permutation test, n = 66, 30. **F)** DNA domains are larger after flavopiridol treatment, as reflected by an increase in $L_{corr}$. *** indicates p<0.001, same statistics as panel C. **G)** In flavopiridol-inhibited cells, DNA domains become proportionally more pronounced with increasing intensity of retained nuclear RNA (for cell selection, see SI Figure 4 D). Mean $C_{DNA}$ of mitotic and interphase control cells given as reference values, quantification based on spinning disk confocal microscopy, individual values with a running mean±SEM. **H)** In cells treated with the transcription inhibitor actinomycin D (Act-D), DNA domains become more pronounced only after 60 minutes, indicated by a $C_{DNA}$ increase. Images recorded using spinning disk confocal microscopy, individual values with mean±SD, plotted values limited to 22 points, ** indicates p<0.01, *** p<0.001 for differences in mean compared to the temporally preceding condition, Bonferroni-corrected permutation test, n = 255, 22, 66, 113. **I)** Summary scheme of observations up to this point, for description see main text.

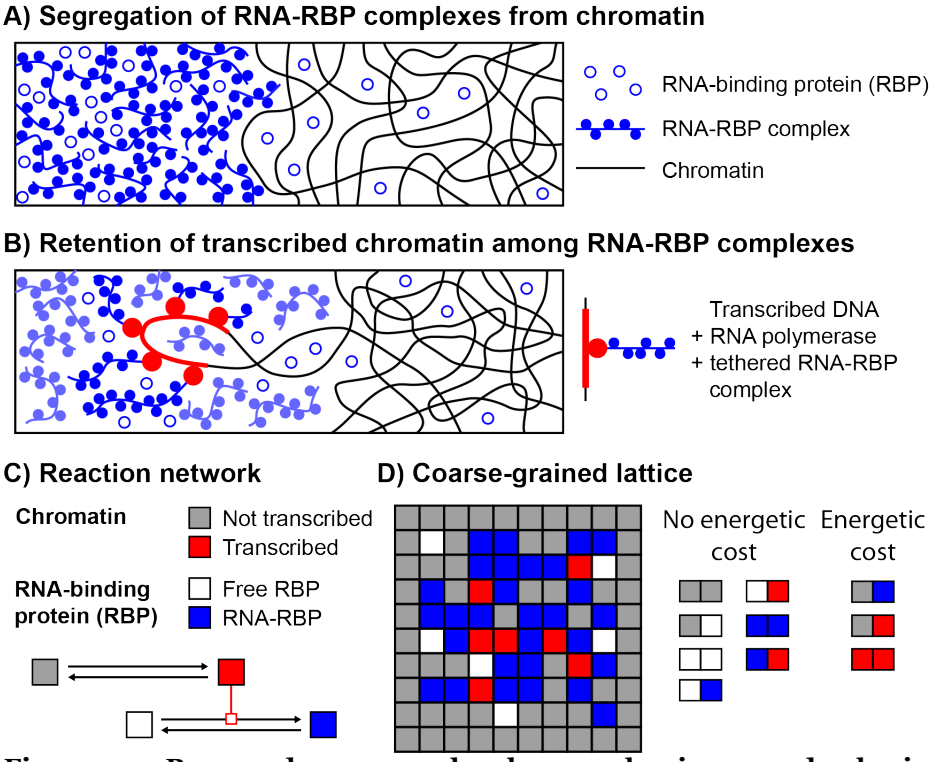


**Figure 3: Proposed macromolecular mechanisms and physical model of euchromatin organization.** We construct a physical model based on two macromolecular mechanisms. **A)** The first mechanism is a segregation of complexes formed between RNA and RNA-binding proteins (RBPs) from chromatin. RBPs not bound by RNA do not segregate from chromatin. **B)** The second mechanism is a localization of transcribed DNA to RNA-RBP-rich regions of the nucleus. This localization occurs due to the tethering of RNA-RBP complexes to transcribed DNA. **C)** The physical model follows two main species, chromatin and RBP. Chromatin can convert between a not transcribed and a transcribed state. RBPs can be either unbound or part of RNA-RBP complexes. The conversion between these states is described by a reaction network. RBP converts into RNA-RBP complex only in the direct neighborhood of transcribed chromatin. **D)** Spatiotemporal dynamics are coarse-grained by introducing a lattice with a resolution of 50 nm, which monitors the concentration profiles of the different macromolecular species. Spatial organization occurs by stochastic swapping of the contents of neighboring lattice sites. The lattice margin is padded with not transcribed chromatin to account for chromatin anchoring at the nuclear envelope. The segregation of chromatin from RNA-RBP complexes is implemented in the form of a free energy cost for swap operations that place RNA-RBP complexes next to chromatin.

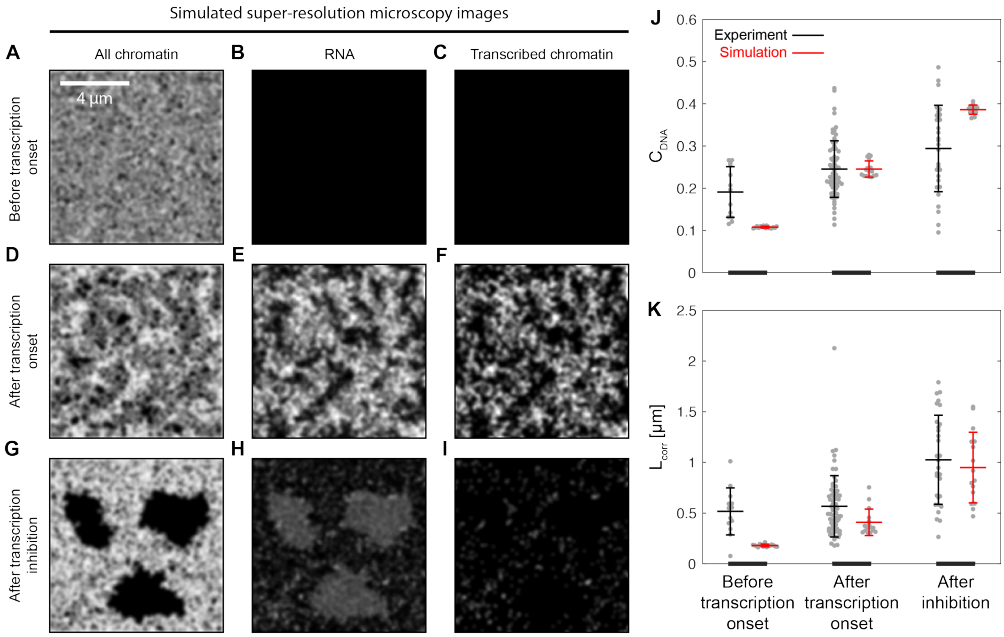


**Figure 4: Simulations of chromatin organization reproduce key features of experimental observations.** To approximate different experimental conditions, simulations using a 10-by-10 µm² lattice (200×200 lattice sites) are executed, followed by the extraction of concentration profiles that can be compared to microscopy images. **A-C)** Simulations that approximate the conditions before transcription onset result in chromatin concentration profiles that do not exhibit distinct domains (A). The concentration of RNA (B) and transcribed chromatin (C) is zero throughout the lattice. **D-F)** Concentration profiles from simulations approximating conditions after transcription onset exhibit chromatin domains (D) and domains containing both RNA (E) and transcribed chromatin (F). **G-I)** Concentration profiles from simulations approximating transcription inhibition show a coarsened pattern of chromatin domains (G) and RNA domains (H). Most chromatin is no longer transcribed (I). **J)** In agreement with experimental results, the DNA image contrast ($C_{DNA}$) in concentration profiles extracted from simulations shows a relative increase from before to after transcription onset, and after transcription inhibition. To correct for differences in background intensity, $C_{DNA}$ values of simulations are scaled to $C_{DNA}$ values from microscopy images in the state after transcription onset. **K)** In agreement with experimental results, the correlation length ($L_{corr}$) of concentration profiles extracted from simulations increases after transcription inhibition. All analyses were carried out for 16 simulations, graphs show individual values with mean±SD.

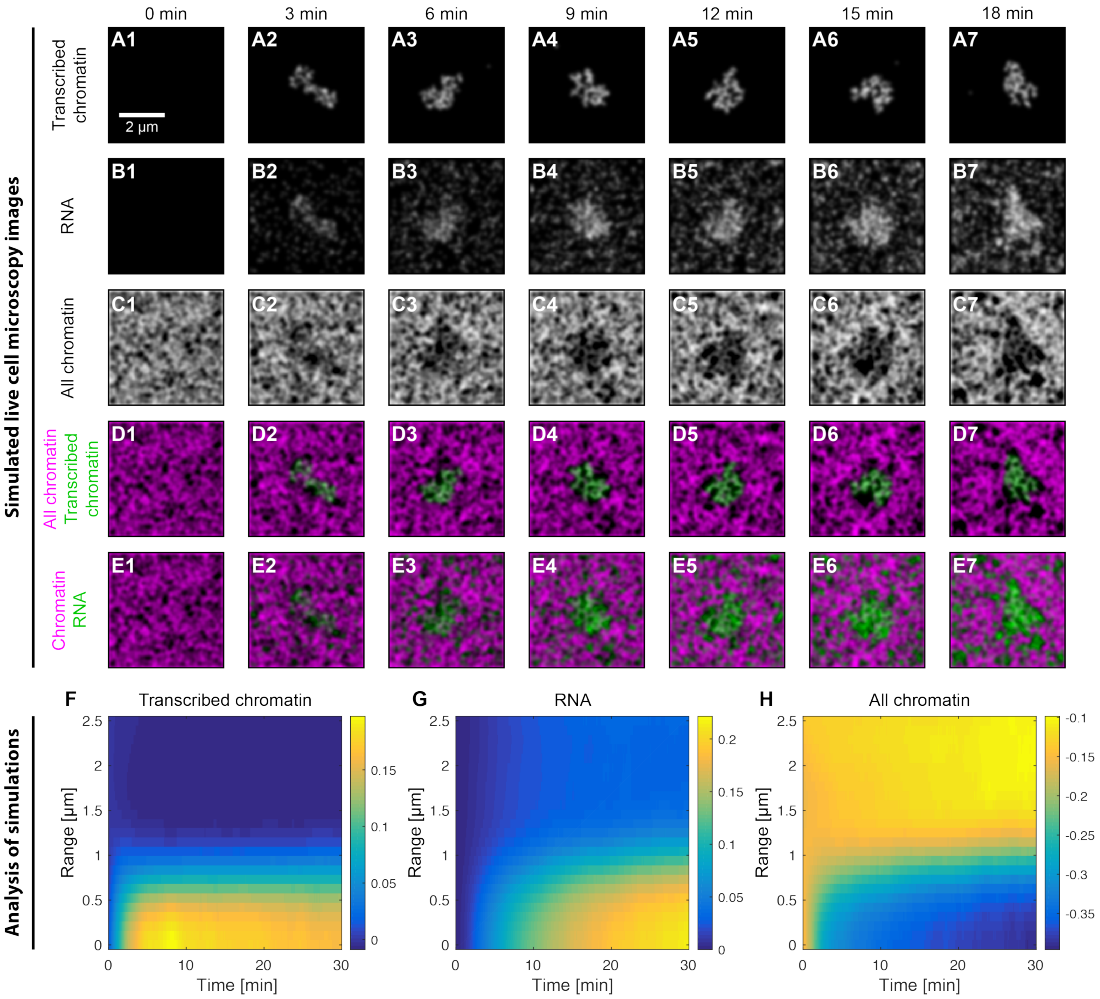


**Figure 5: Dynamics of microenvironment formation in simulations of transcription onset at an isolated transcription site.** The transcription onset at an isolated transcription site in a background of not transcribed chromatin is simulated using a 5-by-5 µm² lattice (100×100 lattice sites). **A**) Time course of concentrations profiles of transcribed chromatin, showing transcription onset at the isolated site. **B)** Corresponding RNA concentration profiles show the establishment and subsequent growth of an RNA accumulation at the transcription site. **C)** Corresponding concentration profiles including all (transcribed and not transcribed) chromatin show the displacement of most chromatin from a growing region at the transcription site. A few pieces of chromatin are retained in the resulting depletion zone. **D)** Two color overlay images show that transcription occurred from the chromatin pieces retained within the depletion zone. **E)** The growing RNA accumulation is confined to the growing chromatin depletion zone. **F-H)** Radial analysis over 30 simulations reveals a consistent spatiotemporal coordination between transcription onset (F), RNA accumulation (G), and chromatin depletion (H) at the activating transcription site. In the radial analysis plots, a range of 0 refers to the centroid of the transcribed chromatin concentration profile. The analysis range is radially extended to shells emanating out from the centroid position. Time is measured after the first detection of transcriptional activity. Concentration values are background-subtracted, leading to negative values in some cases.

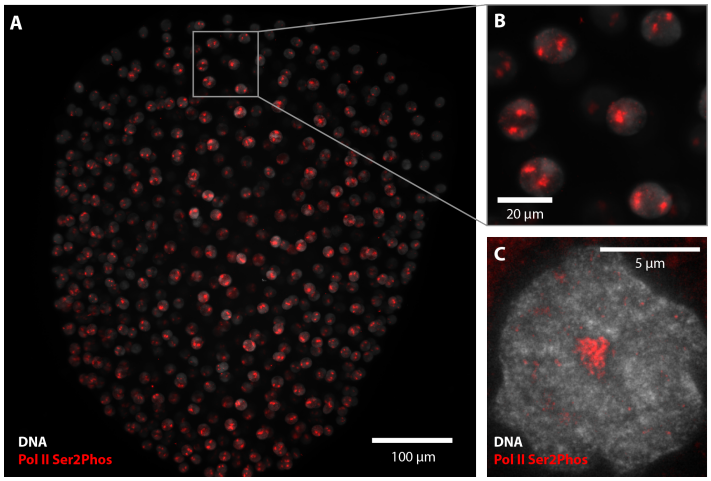


**Figure 6: Two prominent transcription sites consistently precede nucleus-wide transcription. A)** Light sheet micrograph showing the occurrence of two prominent transcription sites (Pol II Ser2Phos) in the nuclei of a fixed late blastula zebrafish embryo (animal view, maximum intensity projection). **B)** Detail showing the occurrence of two prominent transcription sites per nucleus. **C)** STED microscopy section from a nucleus before nucleus-wide transcription onset, showing an isolated transcription site.

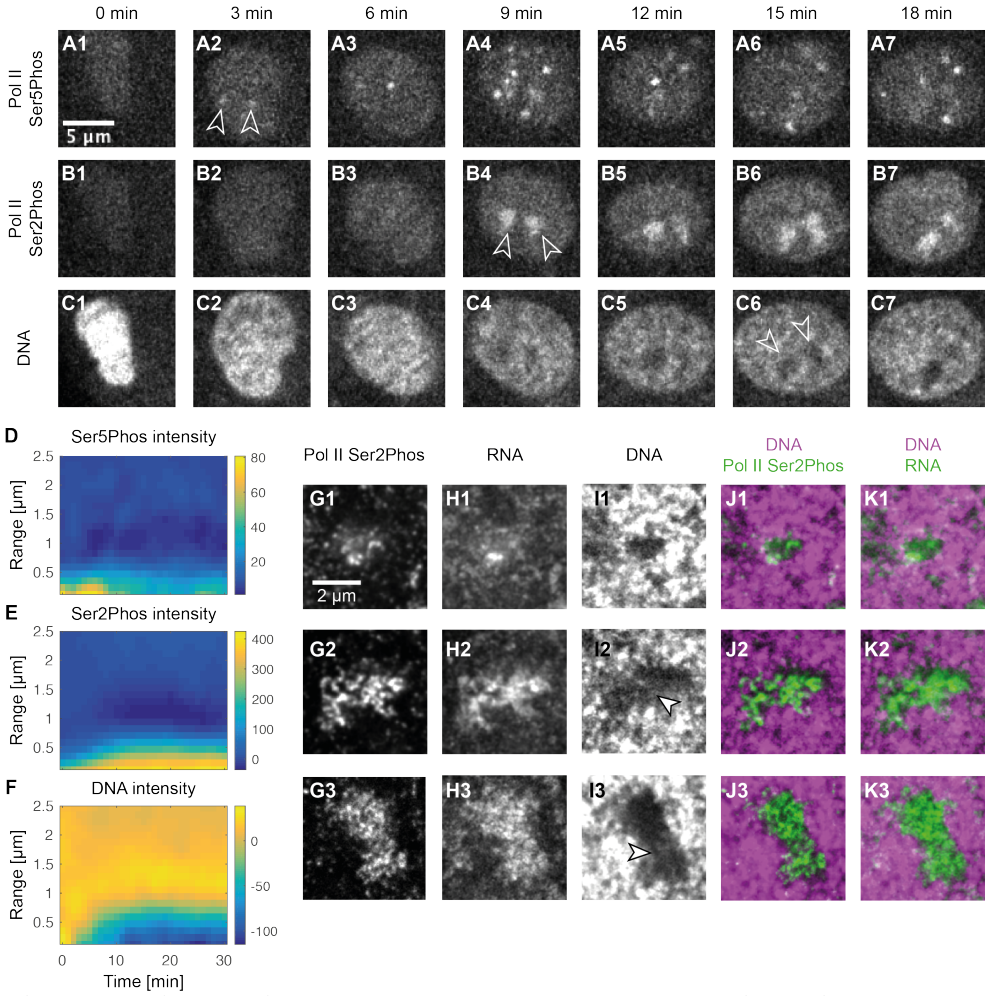


**Figure 7: Microenvironments form by RNA accumulation, displace not transcribed chromatin, and retain transcribed chromatin. A**) Microscopy time course showing the recruitment of RNA polymerase II to two sites shortly after mitosis (arrowheads), followed by RNA polymerase II recruitment at multiple sites several minutes later. Polymerase recruitment was visualized by Pol II Ser5Phos antibody fragments. Images are z-sections. **B)** Two recruitment sites develop strong transcription elongation signal (arrowheads). Elongation was monitored by Pol II Ser2Phos antibody fragments. **C)** DNA is displaced from these two prominent sites of elongation, forming a DNA depletion zone (arrowheads). DNA was labeled with SiR-DNA. **D-F)** A radial analysis covering the two prominent transcription sites of 13 nuclei shows a conserved sequence of conversion from Pol II Ser5Phos (D) towards Pol II Ser2Phos (E) and spatiotemporally coordinated DNA depletion at the transcription site (F). A range of zero refers to the centroid of a given transcription site. The time axis begins when major foci are first detectable in the Pol II Ser2Phos channel. Intensities are in arbitrary units. Negative intensity values result from background-removal. **G)** Transcriptional activity intensity images of STED microscopy sections through prominent transcription sites, ordered by increasing transcriptional activity (G1 to G3, monitored by Pol II Ser2Phos). **H)** Corresponding RNA intensity images, showing the RNA accumulation. **I)** Corresponding DNA intensity images, showing displacement of DNA from a growing depletion zone. Low intensity signal for DNA is retained within the depletion zone (arrowheads). **J)** Color merge showing the localization of transcriptional activity in the growing DNA depletion zone. **K)** Color merge showing that the RNA accumulation is confined in the growing DNA depletion zone.

## Supplementary Figures

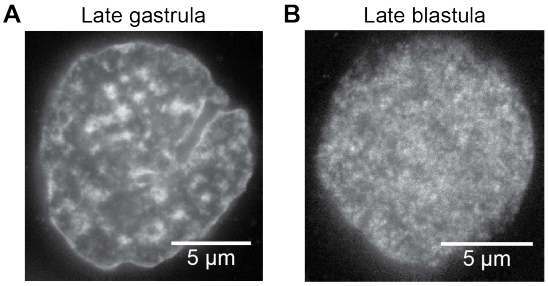


**SI Figure 1: Heterochromatin domains are not observed at the zebrafish late blastula stage.** In an electron microscopy study of mouse embryos, it was found that heterochromatin is not present during blastula stages, but only with progressing gastrulation (Ahmed *et al.*, 2010). Ahmed and colleagues identified heterochromatinization based on the observation of highly compacted DNA domains. Following this approach, we assessed heterochromatin domain formation by STED super-resolution microscopy of SiR-DNA-labeled DNA. **A)** Representative interphase nuclear mid-section from an 80% epiboly embryo (80% epiboly is a late stage of the gastrula period). The nuclear mid-section shows highly compacted DNA domains comparable to heterochromatin domains shown by Ahmed and colleagues. **B)** Representative interphase nuclear mid-section from a late blastula embryo. In late blastula nuclei, compacted DNA domains comparable to the ones observed at 80% epiboly were never observed. Following Ahmed and colleagues, we take this as indication of the absence of heterochromatin.

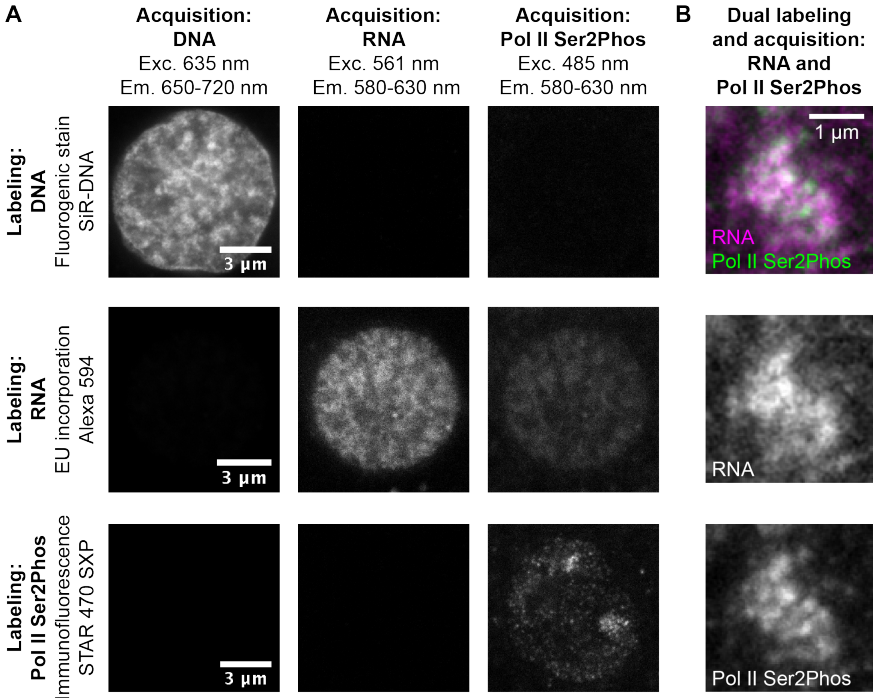


**SI Figure 2: The distributions of DNA, RNA, and transcriptional activity can be assessed by three-color STED super-resolution microscopy.** We used a STED microscopy approach that allowed the acquisition of three different fluorescence labels in the same sample, and using the same STED depletion laser (775 nm). Specifically, DNA was labelled with the fluorogenic DNA stain SiR, which is based on fluorophore silicon rhodamine fluorophore. RNA was tagged by the incorporation of 5'-ethynyl uridine injected at the 1 cell stage, and click-labeled with Alexa 594. Pol II Ser2Phos was labeled by indirect immunofluorescence using the long Stokes shift fluorophore STAR 470 SXP, which can be excited with a 488 nm laser, can be detected in the ~600 nm range, and responds to depletion by the STED laser. **A)** To assess if the signals for DNA (SiR-DNA), RNA (EU with Alexa 594), and transcriptional activity (immunofluorescence against Pol II Ser2Phos with STAR 470 SXP) can be separately acquired without crosstalk, we prepared samples in which only one of the three labels was applied (indicated on left side). We acquired from each of these samples three-color micrographs of at least three nuclei, and show one representative micrograph for each sample. SiR-DNA and STAR 470 SXP signal exhibited no cross-talk outside the intended acquisition channel. Slight cross-talk from labeled RNA to the acquisition channel intended for Pol II Ser2Phos. **B)** To assess the relevance of the cross-talk from the RNA label to the Pol II Ser2Phos acquisition channel, we compared the patterns in a sample with both labels. We find that there are regions with high signal in the RNA image that do not occur in the Pol II Ser2Phos image. This indicates that intensity distributions in the Pol II Ser2Phos acquisition channel result largely from actual Pol II Ser2Phos staining that significantly exceeds cross-talk from the RNA label. Hence, intensity distributions observed in the Pol II Ser2Phos acquisition channel are unlikely to be unintended detection of the RNA label.

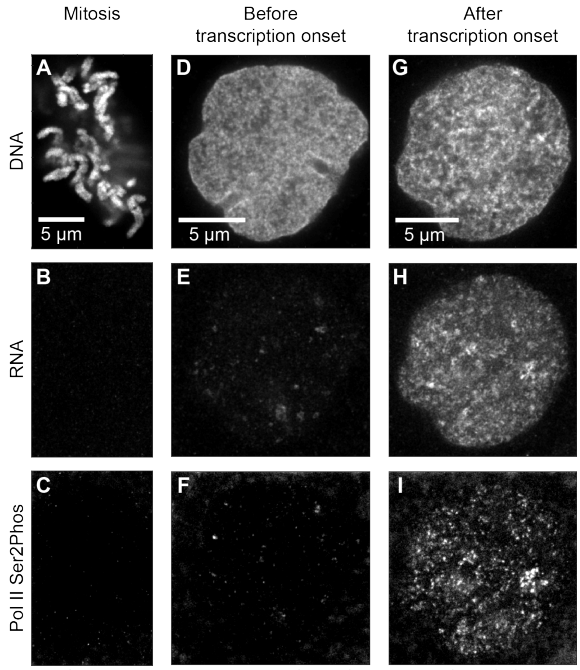


**SI Figure 3: After mitosis, no significant RNA accumulation or transcriptional activity is detected in the nucleus. A-C)** STED super-resolution mid-section of the nucleus of a late blastula cell during mitosis, as indicated by DNA condensation (A). No signal for nuclear RNA (B) or transcriptional activity (C, monitored by Pol II Ser2Phos) is apparent. **D-F)** Nuclear mid-section from a cell shortly after mitosis (D), showing only minimal nuclear RNA (E) and transcriptional activity (F). **G-I)** Nuclear mid-section from a cell in interphase (G), showing nuclear RNA accumulation (H) and transcriptional activity (I). All nuclei recorded from the same sample; acquisition settings and intensity maps are kept the same across all imaged nuclei.

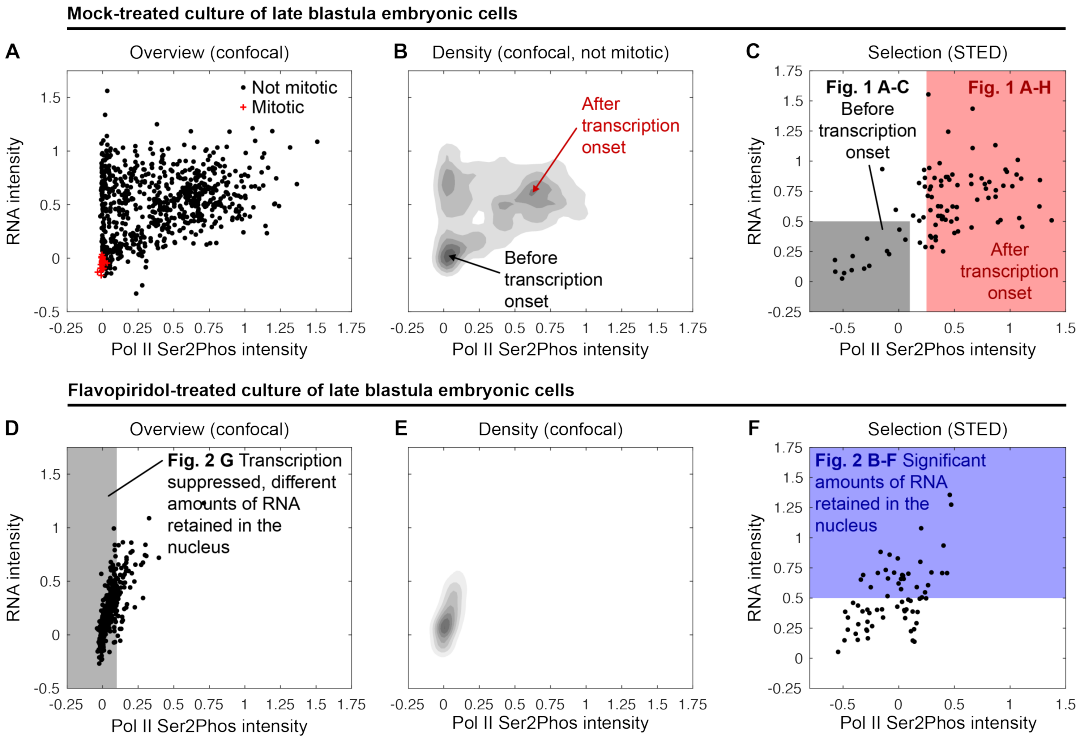


**SI Figure 4: Selection of cells for image analysis.** To select cells in specific states, we first mapped out cell populations based on spinning disk confocal microscopy data, detected states of interest in density plots, and used these states as a guidance for cell selection from STED microscopy images. **A)** We quantified the transcriptional activity (monitored by Pol II Ser2Phos) and amount of RNA accumulated in the nuclei of mock-treated late blastula cells from spinning disk confocal microscopy images. Spinning disk confocal microscopy allowed the acquisition and analysis of a number of nuclei high enough to map out the distribution of cells with respect to transcriptional activity and amount of nuclear RNA. Pol II Ser2Phos and RNA intensity values are given after subtraction of cytoplasmic intensity, and are normalized by the mean of the most intense 10% of nuclei. Mitotic cells were labelled based on DNA condensation into distinguishable chromosomes. **B)** Empirical probability density of non-mitotic data points in panel A, showing peaks before and after transcription onset. **C)** For detailed spatial analysis, nuclear mid-section images were acquired by STED super-resolution microscopy. Nuclei before and after transcription onset were selected as indicated by the shaded regions. Pol II Ser2Phos intensity and RNA intensity are given after subtraction of cytoplasmic intensity and are normalized by the 10 most intense nuclei for a given experiment. Data points result from 4 independent samples processed in two experiments. **D)** In flavopiridol-treated cells transcriptional activity is suppressed, as indicated by a lower Pol II Ser2Phos intensity. A range of nuclear RNA amounts persists after transcription inhibition. Images acquired by spinning disk confocal microscopy. Nuclei retained for the analysis of the influence of nuclear RNA are indicated by the shaded region. Intensities were normalized by values obtained in control samples processed in the same experiment, shown in panel A. Flavopiridol has the known effect of suppressing entry into prophase, and in consequence mitosis, so that no mitoses were detected. **E)** Empirical probability density of data points in panel D. **F)** Nuclear mid-section STED microscopy images that show a significant amount of RNA in the nucleus after flavopiridol inhibition were selected for analysis, as indicated by the shaded region. Pol II Ser2Phos and RNA intensities are normalized by the values obtained for the control samples processed in the same experiments, shown in panel C. Data points result from 4 independent samples processed in two experiments.

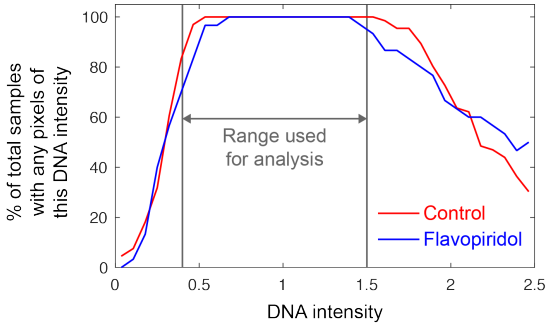


**SI Figure 5: Determination of reliable DNA intensity range.** Here, we determined the range of DNA intensity that could justifiably be used for quantitative analysis of STED microscopy images. To this end, we calculated, for different DNA intensities, the percentage of samples that contained at least one pixel of a given DNA intensity within the cell nucleus. Based on this percentage, we chose a DNA intensity range from 0.4 to 1.5. Outside of this range, a significant drop in the percentage of samples occurs, indicating that analysis in these regions would not be representative of the overall sample population. The Control and the Flavopiridol samples are those described in SI Figure 4 C and F. DNA intensities are normalized within each microscopy image by the mean DNA intensity inside the cell nucleus.

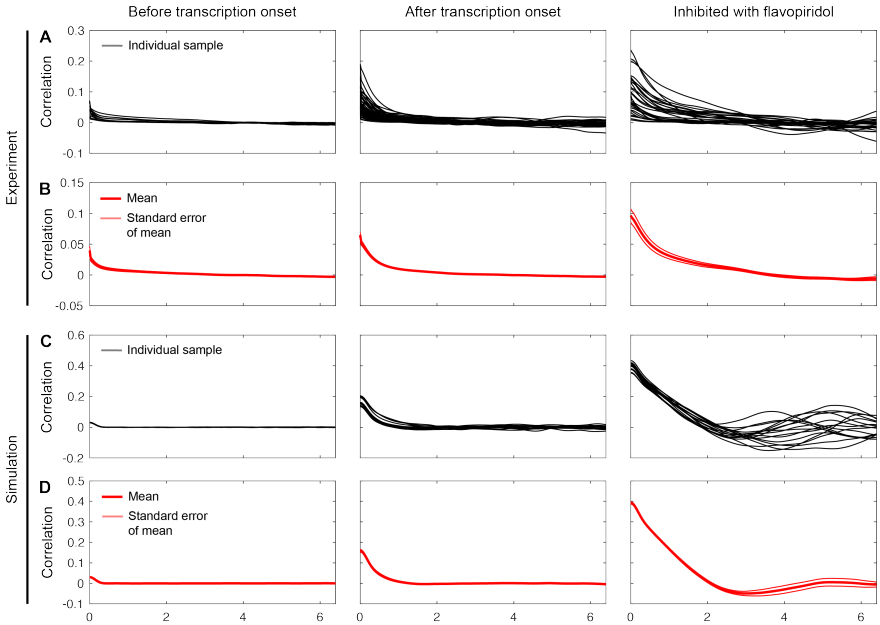


**SI Figure 6: Radial intensity correlation functions used in the correlation length calculation.** To determine the extent of long-range organization of chromatin, the radial correlation functions of the DNA intensity inside of recorded and simulated nuclear mid-sections were calculated. These correlation functions were fitted with an exponential decay function, whose characteristic decay length is the correlation length (procedure not shown in the images). **A**) Correlation functions from individual nuclear mid-sections recorded by STED microscopy in the indicated cell states. **B)** Mean correlation functions of nuclear mid-sections recorded by STED microscopy, with SEM, n=13, 66, 30 individual images. **C)** Correlation functions from individual simulations of nuclear mid-sections in the indicated cell states. **D)** Mean correlation functions of simulated nuclear mid-sections, with SEM, n=16 simulations.

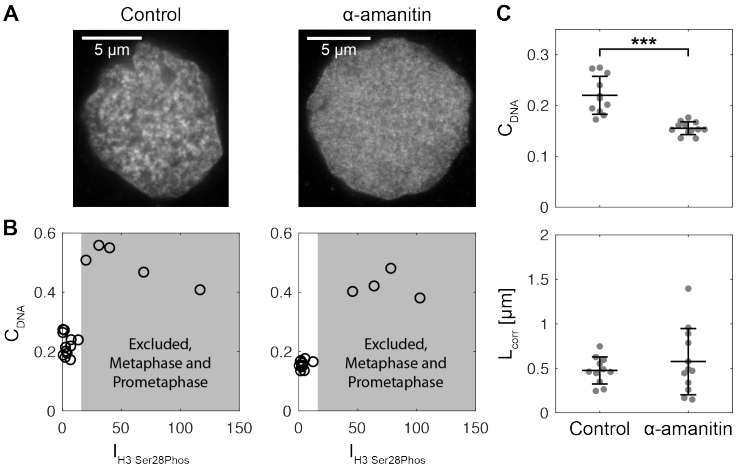


**SI Figure 7: Transcription inhibition with α-amanitin suppresses the formation of DNA domains.** To assess the role of transcription in the formation of DNA domains, we suppressed transcription by injecting the RNA polymerase-specific transcription inhibitor α-amanitin at the single cell stage of embryonic development. Embryos were dissociated at the late blastula stage, cells cultured for 30 minutes, then fixed and labeled. **A)** Nuclear mid-section images acquired by STED microscopy from control-injected embryos exhibited the typical DNA domain pattern observed after transcription onset. In nuclear mid-section images from α-amanitin-injected embryos, no DNA domains were observed. **B)** To exclude cells cells undergoing chromosome condensation in prophase, cells were sorted by the nuclear intensity of Histone 3 Serine 28 Phosphorylation ($I_{H3\ Ser28Phos}$), a common marker for prophase. We excluded cells with significant $I_{H3\ Ser28Phos}$ from further analysis as indicated. **C)** The lack of DNA domains after α-amanitin injection was reflected by decreased DNA image contrast ($C_{DNA}$) relative to nuclei from water-injected embryos. Correlation length ($L_{corr}$) values did not differ, as expected from the observations before transcription onset (Figure 1 C). Individual $C_{DNA}$ and $L_{corr}$ values with mean±SD; *** $p<0.001$ for difference of means, Bonferroni-corrected permutation test, n = 11, 12.

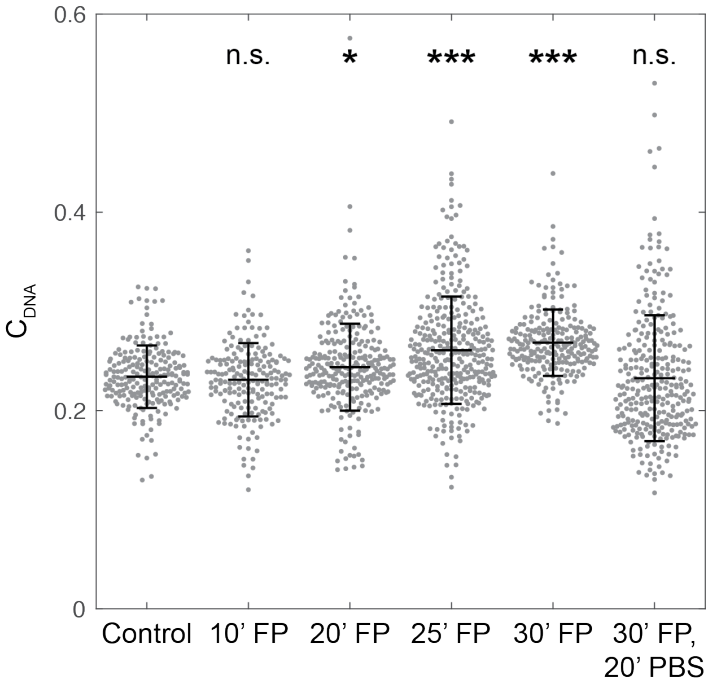


**SI Figure 8: Chromatin compaction due to transcription inhibition with flavopiridol is rapid and reversible.** To assess how quickly flavopiridol induces chromatin compaction and how quickly this compaction can be reversed, we subjected cell cultures to differently timed inhibition sequences. As a reference point, we cultured cells in PBS for 30 minutes (Control). To test the kinetics of chromatin compaction, we replaced the PBS with PBS+flavopiridol for the last 10, 20, 25, or the full 30 minutes of this incubation time (FP conditions with minutes of treatment indicated in graph). To test recovery from 30 minutes of flavopiridol treatment, we replaced the culture medium again with PBS not containing flavopiridol and continued the culture for an additional 20 minutes (30' FP, 20' PBS). We found that DNA compaction, assessed by increasing DNA image contrast ($C_{DNA}$), began at 20 minutes of flavopiridol treatment, increased until 30 minutes of treatment, and was reversed after 20 minutes of washing out flavopiridol. Individual values with mean±SD; n.s. indicates $p>0.05$, * indicates $p<0.05$, *** indicates $p<0.001$ for differences relative to the Control condition, Bonferroni-corrected permutation test, n = 214, 192, 269, 342, 239, 300. All images were recorded by spinning disk confocal microscopy.

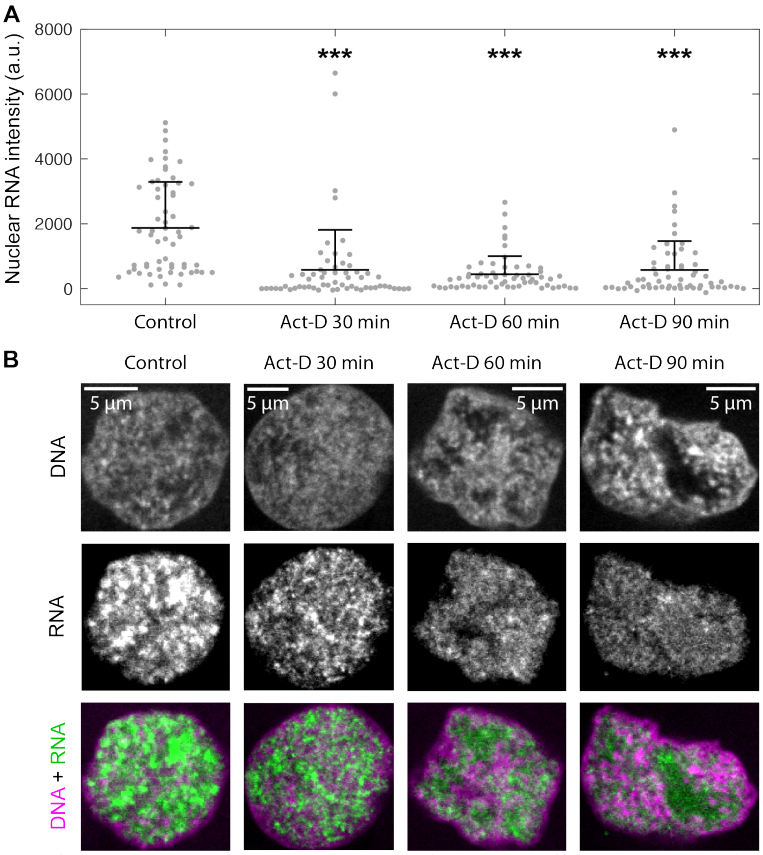


**SI Figure 9: Effect of transcription inhibition with actinomycin D.** Dissociated cells were cultured in PBS for 30 minutes (Control) or PBS+actinomycin D (Act-D) for 30, 60, or 90 minutes. **A)** Act-D treatment uncouples the Ser2 phosphorylation of RNA polymerase II from elongation activity. We could therefore not rely on Pol II Ser2Phos as an indicator of transcriptional activity in this experiment, and instead used a reduction of the amount of RNA in the cell nucleus as an indicator of effective transcription inhibition. Indeed, nuclear RNA intensity is significantly decreased after 30 minutes Act-D and thereafter, indicating rapid and effective suppression of transcriptional activity by Act-D. Individual values with mean+SD. *** indicates $p<0.001$ for differences to the control condition, Bonferroni-corrected permutation test, n = 255, 60, 178, 486; for plotting number of points was capped at 60. **B)** Example nuclear mid-sections showing DNA and RNA intensity profiles, and a color merge of both profiles. After 30 minutes of Act-D treatment, the DNA domain pattern appears unchanged. The amount of nuclear RNA is reduced, but distinct foci of RNA are retained. After 60 minutes Act-D, DNA domains are more pronounced and RNA foci are abolished. This change is more pronounce after 90 minutes. These observations suggest that the retention of transcripts after the application of Act-D prevents the coarsening of the DNA domain pattern. Images were recorded by spinning disk confocal microscopy.

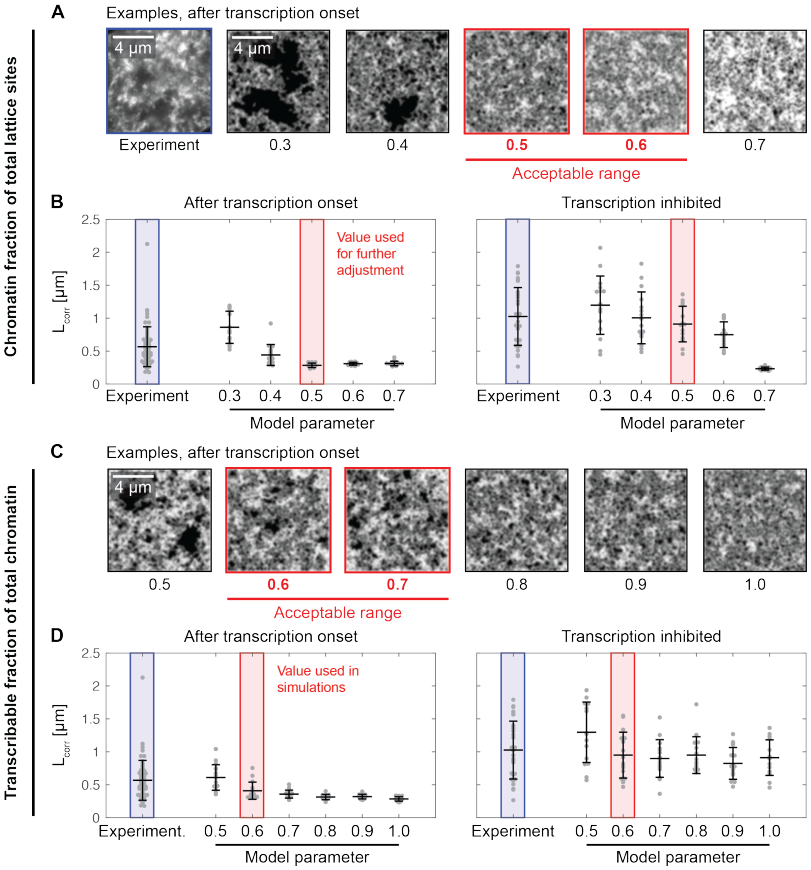


**SI Figure 10: Choice of total chromatin fraction and transcribable chromatin fraction in the physical model.** In our coarse-grained physical model, the fraction of lattice sites occupied by chromatin as well as the fraction of chromatin that can be transcribed need to be chosen. To this end, we execute simulations with different values of these model parameters, and compare the resulting chromatin concentration profiles to our microscopy results. **A)** As a first step, we execute simulations with different total chromatin fraction, while keeping the transcribable fraction at 1.0. A visual assessment of concentration profiles after transcription onset indicates that fractions of 0.5 and 0.6 are in acceptable. Below 0.5, large zones without any chromatin occur, which do not reflect the microscopy image. Above 0.6, the chromatin is too dense to permit formation of low chromatin concentration regions, which are observed in microscopy images. **B)** An assessment of the correlation lengths ($L_{corr}$) of the chromatin concentration profiles from model simulations indicates that 0.5 as well as 0.6 would be acceptable chromatin fractions. We choose 0.5 as a value to use in our simulations. Values from 16 individual simulations are shown with mean±SD. **C)** For further adjustment, we keep the chromatin fraction at the chosen value of 0.5, and produce chromatin concentration profiles for different values of the transcribable fraction. Visual assessment indicates that transcribable fractions of 0.5 and 0.6 are acceptable. Below 0.5, large regions without chromatin occur, which do not agree with microscopy images. Above 0.7, the chromatin concentration profile looks too smooth compared to microscopy images. **D)** Lowering the transcribable fraction towards 0.5 brings $L_{corr}$ after transcription onset closer to experimental values, so that we choose the lowest acceptable transcribable fraction, which is 0.6. Values from 16 individual simulations are shown with mean±SD.

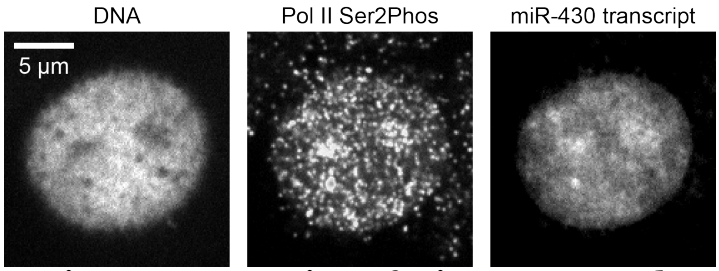


**SI Figure 11: Transcripts of miR-430 are produced within the two prominent transcription sites.** Nuclear mid-section of a late blastula cell. Two prominent depletion zones can be seen in the DNA channel as well as two prominent sites of transcriptional activity (monitored by Pol II Ser2Phos) and two accumulations of primary miR-430 transcripts. Images acquired by spinning disk confocal microscopy.

# Supplementary Methods and Materials

## List of contents

### Embryo dissociation and cell culture

Wild type zebrafish (TLAB) were maintained and raised under standard conditions. Embryos were obtained by natural mating. Embryos were dechorionated within 20 minutes of fertilization and kept at 28.5°C. For dissociation into single cells, embryos in the late Oblong stage were immersed in 1 ml of deyolking buffer (10% v/v glycerol/$H_2O$ with 55 mM NaCl, 1.75 mMKCl, 1.25 mM $NaHCO_3$) in low retention microcentrifuge tubes and vortexed at low speed until no intact embryo fragments could be observed. After centrifugation (1 min, 300 g), supernatant was aspirated and replaced with wash buffer (10% v/v glycerol/$H_2O$ with 110 mM NaCl, 3.5 mM KCl, 2.7 mM $CaCl_2$, 10 mM Tris/Cl, pH 8.5), and tubes were vortexed at low speed to dissolve the cell pellet. After centrifugation (1 min, 300 g), supernatant was aspirated and replaced with 1 ml of PBS (all PBS in this study was Dulbecco's formulation) with 0.8 mM $CaCl_2$ added. Cells were cultured in this suspension for 30 min unless a different time is indicated. At the beginning of the time in suspension culture, tubes were briefly vortexed at low speed and then transferred into a rotator to prevent pellet formation. This dissociation procedure was carried out at the late Oblong stage.

### Transcription inhibition

α-amanitin (A2263, Sigma) was dissolved and diluted to 0.2 mg/ml in $H_2O$, and 1 nl of this solution was injected into embryos at the single cell stage to deliver 0.2 ng of α-amanitin (Lee *et al.*, 2013). Control embryos were injected with 1 nl of $H_2O$.

Flavopiridol (F3055, Sigma) was dissolved to 12.5 M (5 mg/ml) in DMSO, and diluted in PBS+0.8 mM $CaCl_2$ to final concentrations of 1 µM for the application in suspension cell culture (Bensaude, 2011). Control cell cultures were kept in medium with corresponding DMSO concentration. Considering that flavopiridol is a rapidly acting and rapidly reversible inhibitor, we assessed its effect on embryonic development. Embryos raised in medium with 1 µM flavopiridol showed the typical developmental arrest before gastrulation. Normal development was resumed when the drug was washed out within an hour after arrest: embryos showed unperturbed muscle twitching, heartbeat, blood circulation, pigmentation, and swimming behavior during their further development.

Actinomycin-D (A1410, Sigma) was dissolved to 1 mg/ml in DMSO, and diluted in PBS+0.8 mM $CaCl_2$ to final concentrations of 5 µg/ml for the application in suspension cell culture (Bensaude, 2011). Control cell cultures were kept in medium with corresponding DMSO concentration. Because it is known that actinomycin-D is largely irreversible, we did not test reversibility.

### Fixed sample microscopy

*Preparation of fixed cells for fluorescence staining*

To compact the cultured cells into a pellet, suspension cultures were centrifuged during the last minute of cell culture (300 g). To fix the cells

without perturbing the pellet, 8% formaldehyde in 1x PBS was added to the cell culture medium in a volume ratio of 1 in 4, to give an effective concentration of 2% formaldehyde. After 30 minutes of fixation at room temperature, tubes were centrifuged (1 min, 600 g), and supernatant aspirated. To increase the mechanical stability of cells, a secondary fixation step was carried out by applying 8% formaldehyde in PBS for 30 minutes at room temperature, followed by centrifugation (1 min, 800 g) and aspiration. To permeabilize the cell membrane and the nuclear envelope, 0.5% Triton X-100 in PBS was applied for 10 minutes at room temperature, followed by three washes with PBS with 0.1% Tween-20 (PBST).

*Immunofluorescence labeling*

Immunofluorescence labeling started with blocking samples in 4% (w/v) BSA in PBST for 30 min at room temperature. Primary antibodies were diluted in 2% (w/v) BSA in PBST and left to incubate at 4°C overnight. This was followed by three PBST washes at room temperature and subsequent application of fluorophore-conjugated secondary antibodies in the same way as the primary antibodies. Antibodies used in the different experiments are listed in Table 1.

*Total zygotic RNA labeling*

Total zygotic RNA was labeled using the Click-iT RNA labeling kit (C10330, ThermoFisher). 1 nl of 50 µM 5-Ethynyl Uridine (EU, diluted from 100 µM stock in $H_2O$) was injected into the cytoplasm of the first cell following fertilization, so that transcripts produced from the one-cell stage on incorporated EU. Click labeling of incorporated EU with an Alexa-594 azide was carried out following the manufacturer instructions, applying 100 µl click labeling mix per microcentrifuge tube. When combined with immufluorescence staining, click labeling was carried out after permeabilization and before BSA blocking.

*FISH labeling of primary miR-430 transcripts*

miR-430 primary transcripts were labeled by RNA fluorescence *in situ* hybridization (RNA FISH) using a primary transcript probe kindly provided by Antonius van Boxtel (van Boxtel *et al.*, 2015). FISH probes were *in vitro* transcribed from linearized pGEMt_miR-430_ISH plasmid (NdeI restriction enzyme, New England BioLabs) using T7 polymerase (*in vitro* transcription mix: 2 µl transcription buffer (Roche), 2 µl DIG RNA labeling mix (Roche), 2 µl DTT stock (0.1 mM stock concentration), 1 µl RNAse inhibitor (Roche), 8 µl linearized DNA, 4 µl nuclease-free $H_2O$, 1 µl T7 polymerase (produced in-house at Max Planck Institute of Molecular Cell Biology and Genetics), left to incubate at 37°C for 2 hours). *In vitro* transcription was followed by addition of 1 µl Turbo DNase (Ambion), incubation at 37°C for 1 hour, clean-up with QiaGen RNeasy MinElute Cleanup kit, and dilution in hybridization buffer (500 ml formamide; 65 ml 20X SSC, pH 5,0; 10 ml EDTA 0.5 M; 50 mg Torula yeast; 2 ml of 10% Tween-20 (v/v); 5 ml of 20% SDS (manufacturer stock concentration); 2 ml of 50mg/ml Heparin stock, filled up to 1 l, aliquoted to 50 ml, and stored at -20°C) to 50 mg/ml. The FISH procedure was started with one wash 50%/50% (v/v) Methanol/PBST, followed by two

washes with 100% Methanol, then samples were placed at -20°C overnight. After returning samples to room temperature, two washes in 50%/50% Methanol/PBST and 2 washes in PBST followed. 70°C prewarmed hybridization buffer was added and samples were incubated for 1 hour at 70°C. Samples were then incubated in prewarmed hybridization buffer with 1:25 hybridization probe for 4 hours at 70°C, followed by three washes in hybridization buffer (70°C, 20 min each), one wash in 50%/50% (v/v) Methanol/PBST (70°C, 15 min exact), and three washes in PBST (room temperature, 10 min each), and 5% (v/v) blocking buffer (2% blocking reagent (Roche, 1 096 176) in 1X maleate buffer; maleate buffer: 150mM maleic acid, 100mM NaCl, pH 7.5, filter-sterilized, stored at room temperature) in PBST (room temperature, 20 min). Primary antibody incubation (mouse IgM monoclonal anti-Pol II Ser2Phos; Anti-Digoxigenin-POD, sheep Fab fragments) was in 2% BSA in PBST at 4°C for 48 hours, followed by three washes with PBST. FISH probes were revealed using the TSA Plus Cyanine 3 signal amplification kit (Perkin-Elmer), preparing 1 µl Cy3-Tyramide in 25 µl amplification buffer per sample, which was applied for 30 min at room temperature, followed by one wash in PBST. Incubation with secondary antibody (anti-mouse IgM-Alexa 488) was in 2% BSA in PBST at 4°C overnight, followed by three washes in PBST.

*DNA labeling and mounting*

DNA was labeled with DAPI or SiR-DNA (SC007, Spirochrome). DAPI was used for spinning disk confocal microscopy. DAPI was added directly into mounting media immediately before mounting at a concentration of 2 µg/ml. DAPI-stained samples were mounted in VectaShield H-1000, a non-setting liquid mounting medium. SiR-DNA was used for STED microscopy, RNA FISH labeled samples (FISH procedure induced high background on DAPI channel), and spinning disk confocal microscopy (equal or superior performance compared to DAPI). SiR-DNA staining produced no or very low signal in PBS, PBS+DABCO, or VectaShield H-1000. SiR-DNA signal was extremely bright when samples were mounted in glycerol-rich media. However, glycerol induced dissociation of several antibody combinations from the samples, an effect known to occur for some antibodies (Vagenende *et al.*, 2013). Thus, for samples where SiR-DNA and immunofluorescence labeling were combined, immunofluorescence staining was followed by a post-fixation step of 30 min in PBS with 4% formaldehyde, 3 washes in PBST, and a careful but thorough replacement of PBST with ~20 µl of pure glycerol. We then diluted the SiR-DNA stock (1 mM in DMSO) in glycerol of which we spiked 1 µl into every sample immediately before mounting. The dilution of SiR-DNA in glycerol was adjusted so that upon addition addition to the 20 µl mounting medium the desired dilution was reached (for dilutions, see Table 1). Samples were mounted by spotting ~20 µl of mounting medium with resuspended cells onto regular microscope slides, applying #1.5 coverslips, and sealing with nail polish.

*STED super-resolution microscopy of fixed cells*

Measurements were performed on a commercial confocal STED microscope (Abberior Instruments, Göttingen, Germany) with pulsed laser excitation (490 nm, 560 nm, 640 nm, 40 MHz), beam scanning module (line frequency 3 kHz), a pulsed STED laser (775 nm, 40 MHz, spatial light modulator to produce the donut) and single photon counting APD detectors. Multicolor STED imaging with the single 775 nm STED laser was done by using chromatic separation of the fluorophores in combination with line-interleaved (time) excitation and detection. For the 560 nm and 640 nm channels, we used the dyes Alexa 594 and SiR, respectively. For the 490 nm channel, we used the long Stokes shift dye Abberior STAR 470 SXP, which emits in the 560 nm and 640 nm channel and can be effectively depleted by the 775 nm STED laser. To account for direct excitation of the SiR dye by the STED laser, we recorded the 640 nm channel additionally with only the STED laser activated. This channel was then subtracted from the SiR 640 nm channel.

*Spinning disk confocal microscopy of fixed cells*

Commercial spinning disk confocal microscopes were used. Optical parts, illumination settings, and acquisition settings were kept consistent for a given experiment. For a list of microscopy platforms and objectives, see Table 1.

| **Data set** | **Primary labels** | **Fluorescence Labels** | **Imaging Platform** | **Objective** |
|---|---|---|---|---|
| SI Figure 1 | - | SiR-DNA (1:60) | Abberior STED | Olympus UPLSAPO 100XO, NA 1.4 |
| SI Figure 7 | - | Sir-DNA (1:400) | Andor Revolution | Olympus UPLSAPO 100XO, NA 1.4 |
| Figure 1; Figure 2 A-F; Figure 7 G-K; SI Figure 2; SI Figure 3; SI Figure 4 C, F | Rabbit IgG anti-Pol II Ser2Phos (1:200), EU | SiR-DNA (1:60), anti-rabbit IgG-STAR 470 SXP (1:200), A594-azide | Abberior STED | Olympus UPLSAPO 100XO, NA 1.4 |
| Figure 2 G; SI Figure 4 A, B, D, E | Mouse IgM anti-Pol II Ser2Phos (1:1000); EU | DAPI, anti-mouse IgM-A488 (1:1000), A594-azide | Andor Diskovery | Nikon Plan Apo 100X, NA 1.45, Oil |
| SI Figure 7 | Rat IgM anti-H3Ser28Phos (1:1000) | SiR-DNA (1:60), anti-rat IgG-A488 (1:1000) | Abberior STED | Olympus UPLSAPO 100XO, NA 1.4 |
| Figure 2 H; SI Figure 9 | EU | DAPI, A594-azide | Andor Revolution | Olympus UPLSAPO 100XS, NA 1.35 |
| SI Figure 11 | Anti-DIG-POD (1:500), Mouse IgM Anti-Pol II Ser2Phos (1:2000) | SiR-DNA (1:500), TSA Cy3 amplification kit, anti-mouse IgM-A488 (1:1000) | Andor Revolution | Olympus UPLSAPO 100XO, NA 1.4 |

**Table 1: Labels and microscopy equipment used for image acquisition in fixed cells.**

*Light sheet imaging of whole fixed embryos*

Fixed whole embryos were prepared, fluorescently stained, and imaged using a Zeiss Z1 light sheet microscope exactly as described by us in a previous publication (Joseph *et al.*, 2017). Pol II Ser2Phos was labeled by immunofluorescence, using mouse IgM anti-Pol II Ser2Phos primary antibody (1:500) and anti-mouse IgM secondary antibody (conjugated with Alexa 488, dilution 1:1000). DNA was stained by adding 1 µg/ml DAPI during secondary antibody incubation.

*List of antibodies*

Primary antibodies:

- Mouse IgM anti-Pol II CTD Ser2Phos (H5), monoclonal, ab24758 abcam
- Rabbit IgG anti-Pol II CTD Ser2Phos, monoclonal, ab193468 abcam
- Rat IgG anti-H3 Ser28Phos, monoclonal, ab10543, abcam
- Mouse IgG anti-Pol II CTD Ser5Phos (4H8), monoclonal, ab5408, abcam
- Sheep IgG Anti-Digoxigenin Fab fragments, conjugated with horseradish peroxidase, 1207733 Roche

Secondary antibodies:

- Goat anti-mouse IgM, conjugated with Alexa 488, A21042 Thermo Fisher
- Goat anti-rabbit IgG, conjugated with STAR 470 SXP, 2-0012-008-9, Abberior
- Donkey anti-rat IgG, conjugated with Alexa 488, A21208 Thermo Fisher

**Live cell microscopy**

*Preparation of antibody fragments for use in live cell microscopy*

The fluorescently labeled antibody fragments (Fabs) specific to Pol II Ser5Phos and Pol II Ser2Phos were prepared as described previously (Stasevich, Hayashi-Takanaka, *et al.*, 2014; Kimura and Yamagata, 2015). Briefly, monoclonal antibodies specific to Pol II Ser5 and Ser2 phosphorylations were digested with Ficin (ThermoFisher Scientific) and Fabs were purified through protein A Sepharose columns (GE Healthcare) to remove Fc and undigested IgG. After passing through desalting columns (PD MiniTrap G25; GE Healthcare) to substitute the buffer with PBS, Fabs were concentrated up to >1 mg/ml using 10 k cut off filters (Amicon Ultra-0.5 10 k; Merck), Fabs were conjugated with Alexa Fluor 488 (Sulfodichlorophenol Ester; ThermoFisher Scientific) or Cy3 (N-hydroxysuccinimide ester monoreactive dye; GE Healthcare) to yield ~1:1 dye:protein ratio. After the buffer substitution with PBS, the concentration was adjusted to ~1 mg/ml.

*Preparation of live cells for fluorescence microscopy*

Directly following fertilization, zebrafish embryos were pronase-dechorionated and 1 nl of a mix made up of 0.3 µl Alexa 488-conjugated Pol II Ser5Phos Fab, 1.7 µl Cy3-conjugated Pol II Ser2Phos Fab, 0.2 µl 1 mM SiR-DNA, and 0.1 µl 10x Phenol Red was injected into the cytoplasm at the single cell stage. Embryos were grown at 28.5°C and dissociated into single cells at

High stage. These cells were mounted in refractive index matched medium exactly as previously described (Boothe *et al.*, 2017). During the time required to mount the cells and start microscopy, cells had undergone one to two divisions. In intact embryos, during the developmental progression from High to Oblong or Sphere stage, cells also undergo one or two cell divisions. Thus, we acquired live microscopy images from cultured cells that should most closely correspond to cells at the Oblong or Sphere stage in the intact embryo.

*Confocal microscopy of live cells*

Live cell cultures were imaged using the Andor Revolution platform with Borealis extension, equipped with an Olympus silicone oil immersion objective (UPLSAPO 100XS, NA 1.35), recording with a single iXon Ultra 888 EMCCD camera. Image data were acquired for up to 4 cell clones in parallel. A full three-color z-stack could be obtained every minute for all cell clones. Time-lapses were recorded over periods of up to 90 minutes, during which cells continuously displayed cell divisions, suggesting no obvious phototoxicity.

**Image preparation and analysis**

*Software used for image preparation and analysis*

Microscopy image preparation was done using FIJI (Schindelin *et al.*, 2012) and MatLab, the latter relying on the Open Microscopy Environment plugin for image import (Goldberg *et al.*, 2005). Further data processing was carried out in MatLab. Final figures were prepared using Adobe Illustrator.

*Segmentation of nuclei*

The nuclei in STED images are segmented by applying Otsu's method for adaptive thresholding to the DNA channel. In some cases, the resulting segmentation mask contains holes, which are removed by a filling step. Distortion and artifacts from out-of-focus light are seen at the boundaries of nuclei. To remove these imaging imperfections from further structural analysis, the segmentation masks are eroded before further analysis.

Spinning disk confocal microscopy data contain several nuclei and consists of a stack of multiple images in the z direction. An initial segmentation step based on a fixed, manually chosen threshold is applied to the DNA channel to obtain substacks containing individual nuclei. To extract a single image close to the middle of the nucleus in a given stack, the z section with the highest intensity contrast in the DNA channel is selected for further analysis. In this image, the nucleus is segmented using the same approach as described for STED images above. Images from STED and spinning disk confocal microscopy can be analyzed in the same manner from here on.

*Calculation of nuclear intensities*

The mean nuclear intensity of a given color channel is extracted using the nuclear segmentation masks obtained from the DNA channel. These mean nuclear intensities contain contributions from actual nuclear signal and also image background intensity. To remove image background intensity, the

fluorescence in the cytoplasm is determined and subtracted from the total nuclear. The cytoplasmic intensity is determined using a segmentation shell that is created by an outward dilation of the nuclear segmentation mask (Stasevich, Sato, *et al.*, 2014; Joseph *et al.*, 2017).

*Calculation of image contrast*

The DNA image contrast ($C_{DNA}$) is calculated as the root mean square contrast of the individual pixels' intensities ($I_n$) and normalized by the mean intensity, $\bar{I} = \langle I_n \rangle$,

$$C_{DNA} = \frac{1}{\bar{I}} \sqrt{\frac{1}{N-1} \sum_{n=1}^{N} (I_n - \bar{I})^2} = \frac{\sigma_I}{\bar{I}},$$

where $\sigma_I$ is the standard deviation. This is equivalent to the coefficient of variation of $I_n$.

The $C_{DNA}$ of samples prepared, stained, and imaged under comparable conditions and identical settings can be quantitatively compared. To compare between images obtained under different conditions, background intensity correction is required. This is also required when microscopy images and simulated chromatin concentration profiles. An appropriate background correction can be calculated assuming an offset to the individual intensity values,

$$I'_n = I_n + I_{offset}.$$

This leads to a changed image contrast value,

$$C'_{DNA} = \frac{\sigma_I}{\bar{I} + I_{offset}} = a C_{DNA}, a = \frac{\bar{I}}{\bar{I} + I_{offset}}.$$

Thus, assuming of a constant $I_{offset}$, $C_{DNA}$ values obtained under different conditions can be normalized by a reference condition, and relative changes in $C_{DNA}$ can be compared. This approach is used to compare between STED microscopy images and chromatin concentration profiles obtained from simulations. Specifically, the condition "after transcription onset" is used to establish the value of $a$, and the $C_{DNA}$ values obtained from simulations are divided by $a$ before comparison.

*Calculation of correlation length*

The correlation length of the DNA intensity distribution ($L_{corr}$) is determined in two main steps. First, the radial correlation function, $g(r)$, is extracted. We use a definition of the radial correlation function that takes into consideration the segmentation mask covering the inside of the cell nucleus. Considering a DNA pixel intensity image $I_{i,j}$, with the two-dimensional position of the pixel indicated by $i$ and $j$, and an associated segmentation mask $\sigma_{i,j} \in \{0,1\}$, the radial correlation function at a distance $r$ is

$$g_x(r) = \frac{\sum_{i=1,j=1}^{N_x - \frac{r}{l}, N_y} \left( \sigma_{i,j} \cdot I_{i,j} \cdot \sigma_{i,j+r/l} \cdot I_{i,j+r/l} \right)}{\sum_{i=1,j=1}^{N_x - \frac{r}{l}, N_y} \left( \sigma_{i,j} \cdot \sigma_{i,j+r/l} \right)},$$

in the case of shifting in the x direction. Note that, due to the pixel resolution $l$, $g_x\ (r)$ is only evaluated at discrete intervals $r = 0, l, 2l, \dots, N_x l$. The equivalent calculation is carried out for shifts in y direction to obtain $g_y(r)$. The combined radial correlation function then is $g(r) = \left(g_x\ + g_y\ \right)/2$. Before the calculation of *g(r)*, the intensities of all color channels are normalized by the respective color channels' mean intensity in the segmented nucleus, followed by subtraction of the mean intensity in the segmented nucleus.

Second, to obtain $L_{corr}$, an exponential decay function is fitted to *g(r)*. To this end, the function

$$f(r|L_{corr}) = g_\infty + (g_0 - g_\infty) \cdot e^{-\frac{r}{L_{corr}}},$$

is adjusted to *g(r)* by optimization of the value of $L_{corr}$. Here, $g_0 = g(r = 0)$ and $g_\infty$, representing the plateau level of the decaying correlation function, was approximated by the mean value of *g(r)* in the interval of $r$ from 4.5 to 6.0 μm.

A common approach to structural characterization, Fourier analysis, cannot be used. Given that the structural analysis has to be contained to the inside of cell nuclei, domains with irregular boundaries need to be analyzed. It is not clear how Fourier analysis can be applied to such irregular domains in a straight-forward manner.

*Intensity distributions of one color channel with respect to another color channel*

To determine the relationship between the intensity profiles of different color channels, we analyze the distribution of fluorescence intensities of a given channel (A) with respect to intensities in another color channel (B). To this end, all pixels of an image are binned based on the intensities of channel B. Then, the mean intensity on the channel A of all pixels within a given bin is calculated. This analysis reveals the intensity distribution of color channel A with respect to intensities in the color channel B.

The same principle can be applied to resolve a color channel A by the intensities of two other color channels, B and C. Instead of binning pixels only with respect to a single color channel (one-dimensional binning), the pixels are now binned with respect to two color channels (two-dimensional binning).

*Analysis of live cell images*

At every time point, nuclei are segmented based on Pol II Ser5Phos Fab signal. Specifically, we first use the fact that signal of Pol II Ser5Phos Fab occurred in nuclei but also throughout the cytoplasm to segment cells from background using an Otsu threshold. Second, we use the higher signal intensity within nuclei to segment nuclei from cytoplasm, by applying an Otsu threshold within the segmented cells. When the Otsu metric is below 0.65, nuclei are segmented. Otherwise, it is assumed that the Fab pool was released to the cytoplasm due to nuclear envelope breakdown during mitosis, and no nuclei are segmented. For all pixels within segmented nuclei, their 3D distance to the nearest non-segmented pixel is calculated. To segregate nuclei that are too

close to be directly segmented, a water-shed segmentation is initiated from the maxima of this distance map. The segmented nuclei are first automatically tracked through time by their centroid distance. Where tracks have gaps, or are not correctly connected, tracks are then manually corrected.

To analyze spatial organization around the two prominent transcription sites, we carried out a radial intensity analysis that is centered on these. Before any analysis, all fluorescence images are locally corrected for background intensity: each xy image is copied, filtered with a Gaussian kernel (kernel width of σ=2.38 μm), and subtracted from the unprocessed image. Transcription sites are segmented with an Otsu threshold applied to the Pol II Ser2Phos channel, and the two largest objects are retained, assuming that they are the two prominent transcription sites. For both these objects, the centroid is determined, and the xy-section containing the centroid is extracted for radial analysis. Within these xy-sections, the pixel containing the centroid is marked as the starting point of the analysis. With respect to the radial range of the analysis, this pixel is located at a range of 0, referring to the center of the transcription site. The first radial outward step now marks all 8 neighbors of this initial pixel, and refers to a radial range of 1 pixel. A radial range of 2 pixels is reached by marking the next line of outward-lying neighbors, and so forth for all further ranges. At all ranges, the mean intensities of Fab Pol II Ser5Phos, Fab Pol II Ser5Phos, and SiR-DNA signal within the pixels belonging to this radial range is calculated. This procedure produces an intensity curve for all color channels at different radial ranges with respect to the centroid of a given transcription site. To average over the transcription sites of several nuclei, the tracked nuclei were temporally aligned by the first time at which two transcription foci could be detected in a given nucleus. Two-dimensional images of intensity resolved by radial range and time were then created for each tracked nucleus. These were averaged over all tracked nuclei to create final plots.

**Details of the physical model**

Our physical model follows conversions of species by a chemical reaction network, and spatial configuration in a two-dimensional, square lattice with $N \times N$ sites. The chemical reactions are simulated with a constant time step, $\Delta t_{chem} = \frac{0.1}{k_{max}}$, where $k_{max}$ is the maximal reaction rate in the reaction network. In every iteration step, the species present at a given lattice site can only undergo one reaction, see reaction network shown in Figure 3 C. Therefore, for every iteration step, for each site we compare a uniformly distributed random number $r$, with $0 \leq r \leq 1$, to the reaction probability $P_{reaction} = \Delta t_{chem} k_{reaction}$, where $k_{reaction}$ is the rate of a given conversion reaction. When $r \leq P_{reaction}$, the reaction is executed.

Species located at different lattice sites change their location stochastically with direct neighbors. Swap operations are attempted at constant time intervals $\Delta t_{lattice}/N^2$, with $\Delta t_{lattice} \ll \Delta t_{chem}$. For every time step, a lattice site is randomly chosen, followed by random choice of a swap partner from the set

of eight direct neighbors. For these two partners, the potential energy stored in the lattice configuration before and after the swap is calculated, $\Delta E_{swap} = E_{post} - E_{pre}$. $E_{pre}$ and $E_{post}$ are the free energies contained in the local neighbor pairings before and after the proposed swap operation, respectively. The probability of the swap to actually occur is

$$P_{swap} = \exp\left(-\frac{\Delta E_{min} - \Delta E_{swap}}{k_B T}\right),$$

where $\Delta E_{min} < 0$ is the maximally possible free energy release in a single swap. The normalization by $\Delta E_{max}$ ensures that $0 < P_{swap} \leq 1$, and thereby the linearity of time in lattice reconfigurations. The actual free energies of local lattice configurations are calculated from neighbor configurations: every neighboring pair consisting of chromatin/RNA-RBP complex or chromatin/transcribed chromatin imposes an energy cost $w > 0$. Considering all possible neighbor configurations, the maximal free energy release from a swap then is $\Delta E_{min} = -10w$.

To ensure the polymeric integrity of chromatin, a connected components check is executed before every swap operation that involves a chromatin particle. The swap operation is aborted if a breaking of the overall chromatin into an increased number of connected components is detected. The lattice is padded around its margin by stationary chromatin, which allows proper energy calculations at the margins and represents chromatin anchored at the nuclear envelope. Also, swap operations that remove chromatin from the direct neighborhood of the padding chromatin layer were aborted, mimicking anchoring via envelope-attached chromatin.

In our model, the conversion of chromatin from the not transcribed to the transcribed state occurred in two steps. First, the chromatin is divided into subdomains, which represent contiguous gene bodies. These domains can switch between a nontranscribable and an transcribable state. Second, when a given subdomain is in the transcribable state, the individual chromatin sites that are part of the subdomain can transition into the transcribed state (with rate $k^{+}_{Chrom}$). Transcribed chromatin sites can always transition back into the not transcribed state (with rate $k^{-}_{Chrom}$). Subdomains are assigned when the simulation is initialized, by subdividing the chromatin into 1-by-1 μm² subdomains. At the beginning of the simulation all subdomains are in the nontranscribable state. The switching of subdomains into the transcribable state is implemented differently, dependent on the type of scenario that is simulated. In simulations at the whole nucleus level (Figure 4), initially the subdomains are kept off for a number of simulation steps corresponding to 5 minutes real time. Then, for a fraction of 60% of all domains, a non-zero rate of switching into the transcribable state is assigned ($k_{on}$). At all times, the rate for a given subdomain to revert to the nontranscribable state is kept at the same non-zero value ($k_{off}$). To approximate transcription inhibition, all subdomains are again assigned a rate of zero to transition into the transcribable state. In simulations of transcription onset at an isolated transcription site (Figure 5), all subdomains but one are kept in the

nontranscribable state for the entire simulation. A single subdomain in the center of the lattice is assigned as transcribable at the beginning of the simulation. In all scenarios, all chromatin subdomains are monitored as connected components throughout the simulation to maintain their polymeric integrity.

This model was implemented as C++ code (will be released as open source upon publication), which was compiled and executed on the computational cluster of the Max Planck Institute for the Physics of Complex Systems. Concentration profiles of total chromatin and transcribed chromatin were created directly from the respective simulation results. In our microscopy images, RNA signal resulted from a population of RNA not associated with ongoing transcription as well as from high intensity RNA foci that are closely associated with sites of ongoing transcription. We therefore calculated RNA concentration profiles by adding the RNA-RBP complex profile and the transcribed chromatin profile. Their relative contributions were weighted with a factor of 0.2 for the RNA-RBP complex profile and a factor of 0.8 for the transcribed chromatin. To convert the coarse-grained, "all-or-nothing" lattice simulation results into graded concentration profiles, all channels were blurred with a Gaussian filter (kernel width of σ=100 nm).

| Parameter | Property | Value |
|---|---|---|
| $w$ | Reciprocal temperature | 0.15 $k_BT$ [1] |
| $\Delta t_{lattice}$ | Swapping time step | $5x10^{-5}$ min [2] |
| $k_{on}$ | Domain on rate | 0.075 1/min [3] |
| $k_{off}$ | Domain off rate | 0.15 1/min [2] |
| $k^+_{Chrom}$ | Transcription onset | 0.4 1/min [4] |
| $k^-_{Chrom}$ | Transcription termination | 0.1 1/min [5] |
| $k^+_{RNA}$ | RNA production rate | 0.5 1/min [2] |
| $k^-_{RNA}$ | RNA decay rate | 0.05 1/min [6] |

**Table 2: Model parameters.** [1]Lowered relative to the value of $w$=0.5 $k_BT$ from (Larson, Scriven and Davis, 1985) to allow for a sufficiently rapid spatial reorganization in our simulations. [2]Adjusted to achieve sufficient compaction after simulated inhibition compared to our experimental data. [3]Estimated from our live imaging data, using the times from Pol II recruitment (Pol II Ser5Phos) to transcriptional activity (Pol II Ser2Phos). [4]Rate of Pol II escape from promoter-paused state (Stasevich, Hayashi-Takanaka, *et al.*, 2014). [5]Average time of 10 minutes for transcript completion estimated based on a typical length of genes transcribed at late blastula stage of 10 kb (Heyn *et al.*, 2014) and a typical Pol II transcription rate of 1 kb/min (Wada *et al.*, 2009; Jonkers, Kwak and Lis, 2014; Stasevich, Hayashi-Takanaka, *et al.*, 2014). [6]Within the range of typical nuclear retention times of completed transcripts (Bahar Halpern *et al.*, 2015; Battich, Stoeger and Pelkmans, 2015).